Evidence of sub-surface energy storage in comet 67P from the outburst of 2016 July 03

Jessica Agarwal, Vincenzo Della Corte, Paul D. Feldman, Bernhard Geiger, S. Merouane, Ivano Bertini, Dennis Bodewits, Sonia Fornasier, Eberhard Grün, Pedro Henrique Hasselmann, et al.

HAL Id: obspm-02196759

https://hal-obspm.ccsd.cnrs.fr/obspm-02196759v1

Submitted on 3 Dec 2019

Evidence of sub-surface energy storage in comet 67P from the outburst of 2016 July 03

J. Agarwal,[1]★ V. Della Corte,[2,3] P. D. Feldman,[4] B. Geiger,[5] S. Merouane,[1] I. Bertini,[6]
D. Bodewits,[7] S. Fornasier,[8] E. Grün,[9,10] P. Hasselmann,[8] M. Hilchenbach,[1] S. Höfner,[1]
S. Ivanovski,[3] L. Kolokolova,[7] M. Pajola,[11] A. Rotundi,[2,3] H. Sierks,[1] A. J. Steffl,[12]
N. Thomas,[13] M. F. A'Hearn,[7] C. Barbieri,[14] M. A. Barucci,[8] J.-L. Bertaux,[15]
S. Boudreault,[1] G. Cremonese,[16] V. Da Deppo,[17] B. Davidsson,[18] S. Debei,[19]
M. De Cecco,[11] J. F. Deller,[1] L. M. Feaga,[7] H. Fischer,[1] M. Fulle,[20] A. Gicquel,[18]
O. Groussin,[21] C. Güttler,[1] P. J. Gutiérrez,[22] M. Hofmann,[1] K. Hornung,[23] S. F. Hviid,[24]
W.-H. Ip,[25] L. Jorda,[20] H. U. Keller,[26] J. Kissel,[1] J. Knollenberg,[24] A. Koch,[27]
D. Koschny,[27] J.-R. Kramm,[1] E. Kührt,[28] M. Küppers,[5] P. L. Lamy,[29] Y. Langevin,[30]
L. M. Lara,[22] M. Lazzarin,[14] Z.-Y. Lin,[25] J. J. Lopez Moreno,[24] S. C. Lowry,[31]
F. Marzari,[14] S. Mottola,[25] G. Naletto,[6,17,32] N. Oklay,[25] J. Wm. Parker,[12]
R. Rodrigo,[33,34] J. Rynö,[35] X. Shi,[1] O. Stenzel,[1] C. Tubiana,[1] J.-B. Vincent,[24]
H. A. Weaver[36] and B. Zaprudin[37]

Affiliations are listed at the end of the paper

ABSTRACT

On 2016 July 03, several instruments onboard ESA's *Rosetta* spacecraft detected signs of an outburst event on comet 67P, at a heliocentric distance of 3.32 au from the Sun, outbound from perihelion. We here report on the inferred properties of the ejected dust and the surface change at the site of the outburst. The activity coincided with the local sunrise and continued over a time interval of 14–68 min. It left a 10-m-sized icy patch on the surface. The ejected material comprised refractory grains of several hundred microns in size, and sub-micron-sized water ice grains. The high dust mass production rate is incompatible with the free sublimation of crystalline water ice under solar illumination as the only acceleration process. Additional energy stored near the surface must have increased the gas density. We suggest a pressurized sub-surface gas reservoir, or the crystallization of amorphous water ice as possible causes.

Key words: acceleration of particles – scattering – solid state: refractory – solid state: volatile – comets: general – comets: individual: 67P/Churyumov-Gerasimenko.

1 INTRODUCTION

Outbursts are sudden and short-lived events of mass-loss from the surfaces of comets. They have been observed in many comets, on different scales, and under various circumstances. A variety of models have been developed to explain their appearance (Hughes 1990; Belton 2010). Repeating early-morning outbursts at specific sites on comet 9P/Tempel 1 have been attributed to the re-sublimation of

water ice frozen out in the uppermost surface layer during the preceding night, as sublimation in deeper layers would continue during night due to the delay between sub-surface and surface temperature cycles (Prialnik, A'Hearn & Meech 2008b). Outbursts uncorrelated with local time can be driven by cryovolcanism, following the crystallization of amorphous water ice in the deep ($\sim$15 m) interior and the release of trapped CO or CO_2 (Belton et al. 2008). Also, the deepening of a pre-existing crack into layers containing highly volatile material has been proposed as the cause of some outbursts (Skorov et al. 2016). Collapsing sub-surface voids formed by the earlier sublimation of a volatile substance (Vincent et al. 2015) and

collapsing cliffs create dust clouds that can be perceived as outbursts (Steckloff et al. 2016; Vincent et al. 2016; Pajola et al. 2017).

The 2.5-yr *Rosetta* mission at comet 67P/Churyumov-Gerasimenko witnessed a large number of outbursts on various scales. In a catalogue of all optically detected outbursts during the perihelion passage, Vincent et al. (2016) found that the events cluster into two groups by the local time of their appearance: one group occurred in the early morning and was attributed to the rapid change in temperature and resulting thermal stress, the other group was observed in the early afternoon and attributed to the diurnal heat wave reaching a deeper layer enriched in volatiles.

Most outbursts from comet 67P were detected only by a single instrument (Feldman et al. 2016; Knollenberg et al. 2016; Vincent et al. 2016). For many, the approximate source region on the ground could be reconstructed (Vincent et al. 2016), but no systematic search for the traces of the induced surface change has been performed yet, and it might prove difficult in many cases due to the uncertainty of the source region coordinates.

In a few events, *Rosetta* coincidentally flew through the plume of ejected material, while the outburst was also, serendipitously, documented by one or several remote sensing instruments. These events provide particularly valuable data sets due to the nearly simultaneous measurements of several instruments putting strong constraints on the properties of the ejected material and the temporal evolution of the outburst process. Such multi-instrument observations of an outburst on 2016 February 19 were analyzed in Grün et al. (2016). Unfortunately, the location of the site of origin of that outburst could not be derived with certainty. On the other hand, Pajola et al. (2017) could study in great detail the surface change induced by the collapse of a cliff, while only little data on the ejected material were available.

The topic of this paper is an outburst that occurred on 2016 July 03, and was detected by at least five instruments onboard *Rosetta*, such that the quantity, composition and velocities of the ejected material can be derived with some certainty. In addition, the point of origin of this event, its topographic conditions and the induced surface change can be studied in detail due to the serendipitous availability of high-quality images.

In Section 2, we briefly describe the location and timing of the event, followed by detailed accounts of the measurements of the individual instruments and their interpretation. In Section 3, we derive properties of the ejected material and discuss the topography and topographic change at the outburst site. In Section 4, we discuss possible processes to trigger the outburst, and in Section 5, we summarize the key findings and discuss their significance for a larger context.

2 MEASUREMENTS AND THEIR INTERPRETATION BY INSTRUMENT

On 2016 July 03, comet 67P was at a distance of 3.32 astronomical units (au) from the Sun, outbound from its perihelion passage on 2015 August 13. *Rosetta* was in a close orbit about the nucleus, at a distance of 8.5 km from the outburst site that is located inside the circular ($\sim$500 m diameter) Basin F (Auger et al. 2015) in the Imhotep region in the Southern hemisphere of comet 67P, at 172.0° longitude and $-33.2°$ latitude (Fig. 1). The Rosetta instruments contributing to this work and their data concerning the outburst are summarized in Table 1.

A dust plume and its point of origin on the surface were observed by the Ultraviolet Imaging Spectrograph, Alice, beginning
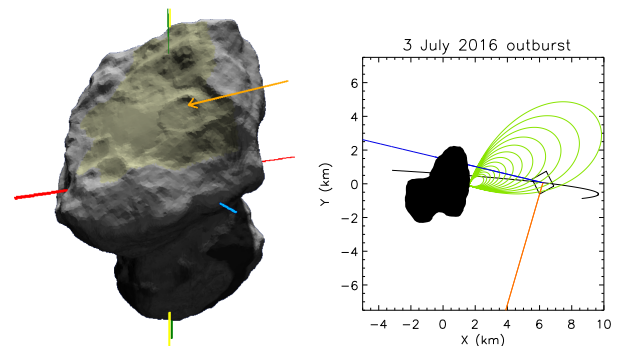

Figure 1. Left-hand panel: location of the outburst site on the comet. The model shows the comet as seen from *Rosetta* on 2016 July 03 at 07:50. The arrow marks the outburst site in the circular Basin F in the Imhotep region (shaded yellow). The yellow lines indicate the comet-Sun line with the Sun at the top of the image. The green, red and light blue lines mark the *x*-, *y*- and *z*-axis of the comet. The south pole is visible where the *z*-axis crosses the comet surface. The image was generated with the CG viewer tool developed by Tim Wittrock (https://planetgate.mps.mpg.de:8114). Right-hand panel: approximate configuration of the plume and the spacecraft. The blue line represents the boresights of the science instruments, and the orange line represents that of STR-B.

Table 1. List of instruments contributing to this work. The first and second columns list the names of the instruments and the type of measurement they perform. The third column lists the type of data contributed to this work.

Name	Type	Data
Alice	Far-Ultraviolet Imaging Spectrograph	Spectrum of the plume
COSIMA	TOF mass spectrometer	Microscope images of 1 fragmented particle
GIADA	Dust detector	Mass and velocity of 22 particles
OSIRIS	Camera system	(Colour-)Images of the outburst site
STR-B	Star tracker camera	Brightness of the diffuse dust background

from 07:36 and by the Wide Angle Camera (WAC) of the Optical, Spectroscopic, and Infrared Remote Imaging System (OSIRIS) at UT 07:50 (Fig. 2). Unless specified otherwise, all further times refer to UT on 2016 July 03. A WAC image of the same region from 07:04 shows the site still in shadow and no sign of dust activity near it. The background radiance of the star tracker camera STR-B began to increase around 07:40, and the Grain Impact Analyzer and Dust Accumulator (GIADA) detected the first particle at 08:26. The peak flux in STR-B and GIADA was observed between 08:40 and 09:00. Material from the outburst was also detected on the dust accumulation targets of the COmetary Secondary Ion Mass Analyzer (COSIMA). An OSIRIS image of the outburst site obtained at 08:48 does not show any obvious dust near the outburst site. GIADA detected the last particle at 10:29, while the background signal of STR-B had not reached its pre-outburst level at 14:00 and continued to decline.

2.1 OSIRIS

OSIRIS (Keller et al. 2007) onboard the *Rosetta* spacecraft comprised a Narrow- and a Wide Angle Camera (NAC and WAC), each with a CCD detector of 2048 × 2048 pixels. The fields of view (FOVs) covered approximately 2° × 2° and 12° × 12°,
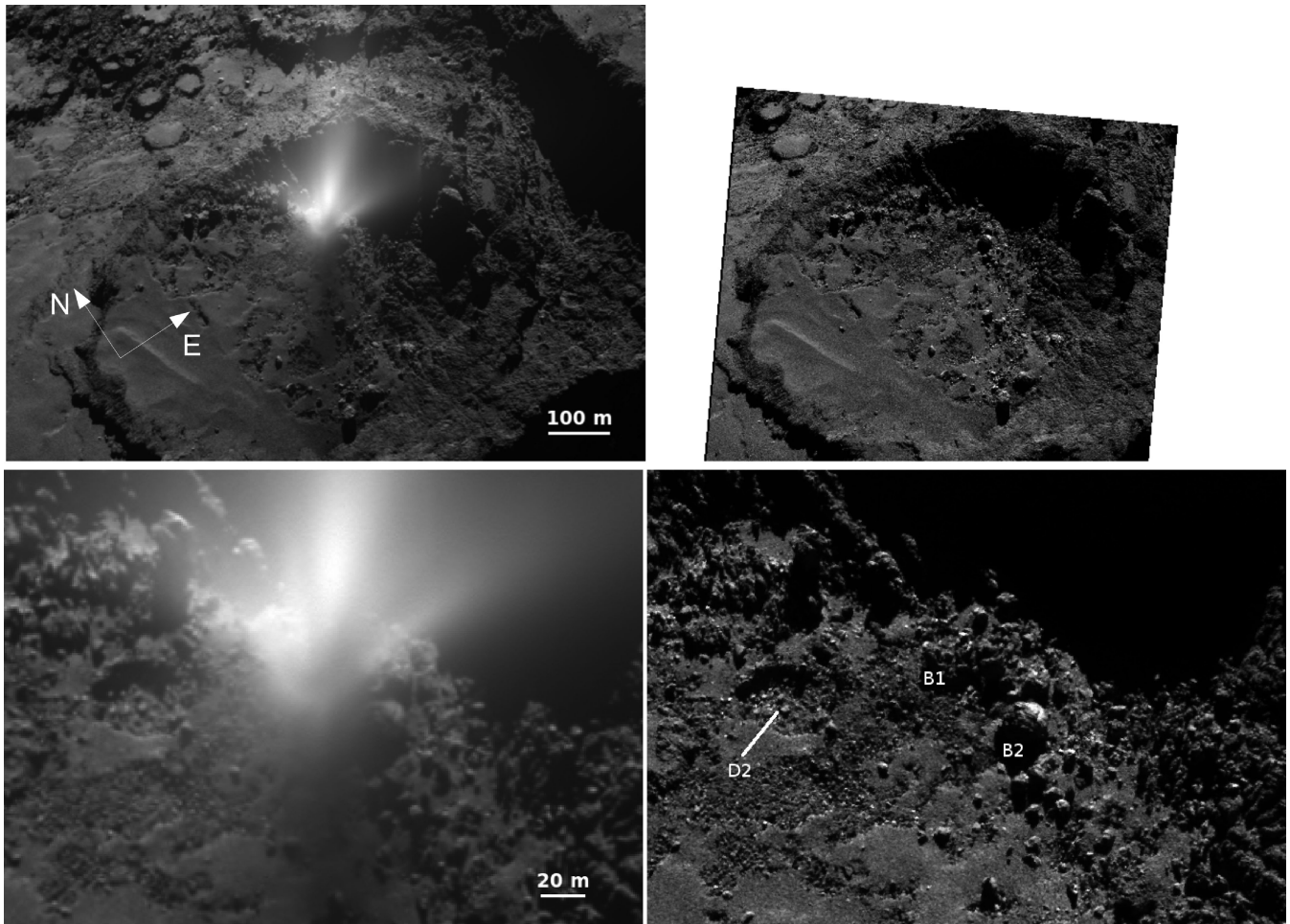
Figure 2. Left: WAC image of the outburst plume obtained on 2016 July 03 7:50. Right: the same region at the same scale and under similar viewing conditions observed with NAC on May 03. The upper and lower rows show the same images at different zoom levels. The boulders B1 and B2, and a neighbouring depression D2, are indicated for orientation and comparison to Fig. 12.

respectively. The cameras were regularly imaging the nucleus and coma of comet 67P/Churyumov-Gerasimenko between 2014 March and 2016 September in 25 broad- and narrow-band filters, covering the wavelength range of 240–1000 nm (Sierks et al. 2015). The standard data processing on ground comprised bias-subtraction, flat-fielding, correction for distortion of the optical path and flux calibration relative to standard stars (Tubiana et al. 2015).

A list of OSIRIS images obtained before, during and after the outburst is given in Table 2, and the properties of the employed filter bands are listed in Table 3. We here analyze images obtained during the last months of the *Rosetta* mission when the spacecraft was close to the comet, providing high spatial resolution.

The dust plume observed by WAC at 07:50 (Fig. 2) was optically thick and cast a measurable shadow on the surface. It originated between two boulders (B1 and B2). The site emerged from the shadow of the northeastern wall of Basin F at 07:30 (local time 10:17). A detailed analysis of this and additional images is found in Section 3.

2.2 Alice

Alice is a far-ultraviolet (70–205 nm) imaging spectrograph onboard *Rosetta* that observed emissions from various atomic and molecular species in the coma of comet 67P/Churyumov-Gerasimenko

(Feldman et al. 2015) as well as reflected solar radiation from both the nucleus and the dust coma (Feaga et al. 2015). Alice employed a two-dimensional photon counting detector that accumulated counts over an interval, usually 5 or 10 min, into a histogram array of wavelength versus spatial position along the 5.5° slit. At the time of the outburst, Alice was obtaining histograms of 604 s integration time. The histogram beginning at 07:37 shows a very large increase in reflected solar radiation in the wide bottom of the Alice slit. From analysis of the OSIRIS image (Fig. 3), we find that the outburst is confined to a region 1.2° × 0.1°, which translates to a projected footprint on the nucleus of 180 m × 15 m. Because of the rotation of the comet and the motion of *Rosetta*, the outburst is seen by the Alice slit for only ~3 min of the 10-min histogram. In comparison to the subsequently obtained spectrum (beginning at 07:47), the spectrum covering the outburst plume shows increased flux at long wavelengths (Fig. 4). The sharp absorption edge below 170 nm is characteristic of sub-micron water ice particles (Hendrix & Hansen 2008). This spectral feature appears only in the histogram beginning at 07:37, and only in the wide bottom of the Alice slit, and thus can be uniquely associated with the plume observed by OSIRIS/WAC 10 min later. Grains in the vicinity of the spacecraft are likely too optically thin to be detected against reflected sunlight from the surface, so we cannot determine if they are water ice. Unlike the outbursts of volatile gas observed by Alice on multiple dates

Table 2. Observational circumstances characterizing the OSIRIS images used for this work. 'C' defines the camera (NAC/WAC). The local time (LT) is calculated as $12 + (\lambda_{site} - \lambda_{sun})/15$, where λ_{site} and λ_{sun} are the longitudes of the outburst site and of the subsolar point in degrees. The azimuth (Az) and zenith distance (ZD) of the spacecraft are given in degrees and were calculated with respect to the vector, r_0, from the origin of the comet reference frame to the outburst site. Az is the angle between the components perpendicular to r_0 of the north direction and the vector, $r_{s/c}$, from the outburst site to the spacecraft. ZD is the angle between r_0 and $r_{s/c}$. The last column gives the distance, D, between the outburst site and the spacecraft in km. Double horizontal lines separate groups of images obtained under similar circumstances. The pixel scale is given by aD, where $a_{NAC} = 18.6$ µrad and $a_{WAC} = 101$ µrad.

Obs. Date [UT]	C	Filter	LT (h)	ZD	Az	D
2016-05-03 00:42	N	Orange	10.9073	53.8	51.1	17.906
2016-07-03 07:50	W	Red	11.0239	48.1	58.9	8.534
2016-07-03 07:04	W	Red	9.4979	38.3	78.0	8.557
2016-07-03 08:47	W	Red	12.9304	68.9	51.9	8.768
2016-07-03 08:50	W	Red	13.0144	69.9	51.9	8.783
2016-07-02 21:26	N	Blue	14.3332	34.2	116.6	11.859
2016-07-02 21:26	N	Orange	14.3395	34.2	116.5	11.857
2016-07-02 21:26	N	NIR	14.3459	34.1	116.4	11.856
2016-07-02 21:36	N	Blue	14.6649	32.9	111.4	11.776
2016-07-02 21:36	N	Orange	14.6712	32.9	111.3	11.775
2016-07-02 21:36	N	NIR	14.6776	32.9	111.2	11.773
2016-03-19 21:26	N	Orange	14.8761	43.4	145.0	10.847
2016-03-19 21:46	N	Orange	15.5388	36.8	140.3	10.746
2016-05-02 12:59	N	Orange	11.5852	54.4	81.2	17.917
2016-05-02 12:59	N	Blue	11.5981	54.4	81.2	17.918
2016-05-02 13:00	N	NIR	11.6276	54.5	81.1	17.920
2016-07-09 20:47	W	Red	11.4596	51.7	106.7	10.317
2016-07-09 21:46	W	Red	13.3904	50.2	90.8	9.938
2016-07-24 10:15	N	Blue	11.0542	51.3	98.0	8.505
2016-07-24 10:15	N	Orange	11.0606	51.2	97.9	8.505
2016-07-24 10:15	N	NIR	11.0670	51.2	97.9	8.504
2016-07-24 10:30	N	Blue	11.5519	50.8	93.5	8.483
2016-07-24 10:30	N	Orange	11.5583	50.8	93.5	8.483
2016-08-21 13:19	W	Red	10.8456	43.9	77.9	7.033
2016-01-06 08:51	N	Orange	8.8523	46.2	34.9	84.652
2016-05-03 12:05	N	Orange	9.5692	46.1	17.3	17.731
2016-05-03 12:25	N	Orange	10.2322	54.9	20.0	17.899

Table 3. List of employed OSIRIS filters and their properties. λ_c: Central wavelength; $\Delta\lambda$: bandwidth; I_{sun}: solar flux at central wavelength and 1 au.

Camera	Filter	λ_c (nm)	$\Delta\lambda$ (nm)	I_{sun} (W m^{-2} nm^{-1})
NAC	NIR	882.1	65.9	0.9230
NAC	Orange	649.2	84.5	1.5650
NAC	Blue	480.7	74.9	2.0300
WAC	Red	629.8	156.8	1.7000

Figure 3. Position of the Alice slit overlaid on the WAC image of the outburst (Fig. 2) as a function of time. The rectangles correspond to individual pixels of the Alice detector, each $0.3° \times 0.1°$, of which rows 4 (green), 6 (red), 8 (blue) and 10 (yellow) are shown. The numbers indicate minutes after UT 07:00, and the white line marks the position of the slit at UT 07:37. The pixel positions were calculated using the pixel centres relative to the central boresight given in the ROS_ALICE_V16.TI instrument kernel in the spice library (Acton 1996).

2.3 Giada

GIADA onboard *Rosetta* was designed to determine the physical properties of cometary dust: momentum, speed, mass and the geometrical cross-section of individual particles (Della Corte et al. 2014, 2016). The information on single particles was derived by two subsystems mounted in cascade: the Grain Detection System (GDS) and the Impact Sensor (IS). The GDS-detected particles crossed a laser curtain, providing their cross-sections and triggering a time of flight (TOF) counter from the GDS to the IS. From this time measurement, the particle speed was retrieved. The IS consisted of a sensing plate equipped with five piezoelectric sensors (PZTs). A particle impacting the sensing plate generated bending waves detected by the PZTs. The PZT signal was monotonically related to the particle momentum. GIADA detections, depending on which sub-system detected the individual dust particle, are divided in (1) GDS-only detections providing the particle cross-section and speed; (2) IS-only measuring particle momentum and (3) GDS-IS detection determining individual particle mass, speed and geometrical cross-section. Since the subsystem detections depend on the particle physical characteristics (size, optical properties, density) thanks to different detection types, we classified different classes of particles. GDS-only detections, occurring as isolated events or as 'dust showers', i.e. up to hundreds of detections in tens of seconds, correspond to ultra-low-density (<1 kg m^{-3}) aggregates (Fulle et al. 2015). IS-only and GDS+IS detections are of compact particles with average density of 800 kg m^{-3} (Fulle et al. 2016).

GIADA detected 22 particles (1 GDS-IS, 10 IS, and 11 GDS) between UT 8:26:29 and 10:29:21 on July 03 (Fig. 5). This detection peek was embedded in a period with almost no other detections. The total number of events during the week from July 01 to 07 was 25, such that 90 per cent of the detected material in this time period are associated in time with the outburst. The peak of detections occurred around UT 09:00, and the particle speeds were typically <3 m s^{-1} (Fig. 6). 50 per cent of the particles were detected by the IS, suggesting that these were compact with bulk densities of order 800 kg m^{-3} (Fulle et al. 2016). It is possible that the detection peak around UT 09:00 and the following decrease in detection rates reflect the temporal evolution of the activity level.

around perihelion (Feldman et al. 2016), no gas emission associated with this event is detected. The Alice housekeeping data, with a time resolution of 30 s, show a rise in the total count rate beginning from 07:36. While this does not necessarily mark the beginning of the outburst due to the motion of the FOV across the comet surface, it represents the latest possible start time.
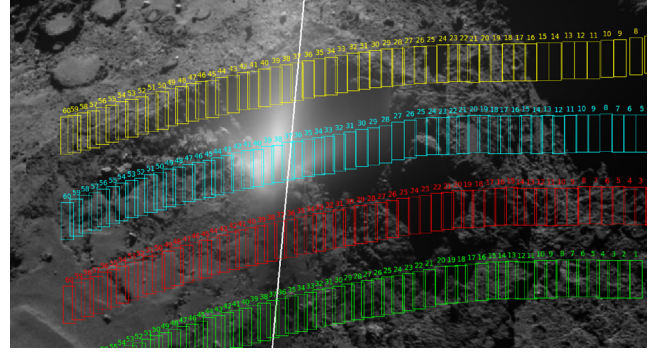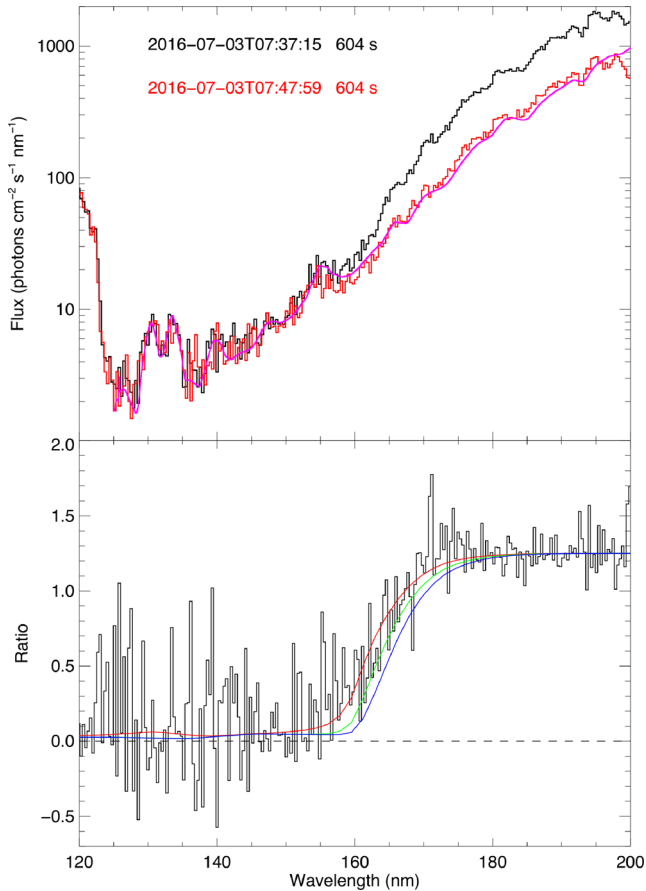
Figure 4. The top panel shows two Alice spectra, each a 604-s integration. The black line histogram begins at UTC 07:37:15, and the peak count rate is determined from the OSIRIS image to occur at ∼07:39. The red line is the following spectrum beginning at UTC 07:47:59, and does not show the long wavelength enhancement due to the outburst but only solar reflected light from the surface. A scaled solar spectrum (McClintock, Rottman & Woods 2005), convolved to the Alice resolution, is shown (in magenta) for comparison. We assume the black spectrum to be that of the outburst grains superimposed on that of the surface, while the red spectrum is surface alone. The difference is then the spectrum of the released grains. The lower panel shows this difference divided by the surface spectrum to give the normalized bidirectional reflectance spectrum. Water ice models with grains of diameter 0.2 μm (red), 0.5 μm (green) and 1.0 μm (blue) from Hendrix & Hansen (2008) are shown. These demonstrate that the grains in this particular outburst are composed of sub-micron water ice particles.

2.4 COSIMA

COSIMA was a TOF mass spectrometer on the *Rosetta* orbiter that collected dust particles in the coma of 67P on substrate frames, with three mounted metallic targets of 1 cm^2 each. With an optical microscope camera, COSISCOPE, the dust particles were imaged with a resolution of 14 μm × 14 μm (Kissel et al. 2007; Langevin et al. 2016). The three metallic targets were exposed at the same time to the cometary dust flux. The typical exposure periods ranged from a few hours up to 3 weeks. Images of the target holder were acquired prior to and after each exposure period. New particles were identified by comparison of the two image sets. The target holder was located at the rear of a 14.9-cm-long funnel with a FOV of 15° × 23°. The cometary particles passed through the funnel before impact on the targets (Fig. 7). The particles collected by COSIMA were able to fragment at very low velocity (Hornung et al. 2016).
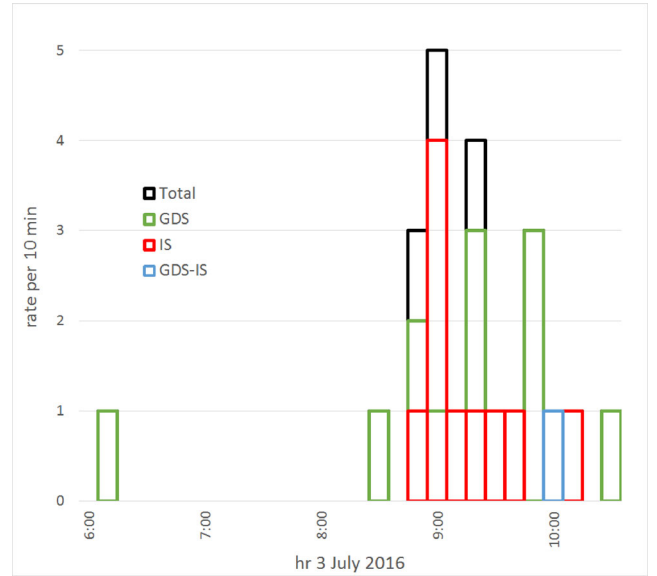
Figure 5. Particle detection rate measured by GIADA. The different event types are colour coded. The one GDS+IS detection occurred at UT 09:56 and revealed a velocity of (1.37 ± 0.08) m s^{-1} and a particle mass of 10^{-7} kg, corresponding to a 310 μm radius sphere of density 800 kg m^{-3}.

Some particles hit the funnel walls prior to impact on the target and likely broke into pieces. These pieces, if they did not stick to the funnel, were scattered and eventually stuck on a target. In order to estimate the number of the primary dust particles that entered the instrument's FOV, this scattering and fragmentation has to be taken into account. To distinguish between individual incoming particles and pieces of particles created by the fragmentation of a larger parent particle, the spatial distribution of the particles collected for each exposure period is analyzed. If the particles are not randomly spatially distributed, they are assumed to come from the fragmentation of a unique parent particle inside the funnel. The method to determine which particles result from such events is described in Merouane et al. (2016).

During the exposure periods preceding as well as following the first week of July, very few particles have been collected (see Table 4). During the week of the outburst, 188 particles were detected on the targets (Fig. 7). However, the analysis of their spatial distribution shows that they are likely to be the fragments of a single large parent particle that disintegrated in the funnel. GIADA detected 22 particles connected in time to the outburst event, with only two other particles within a week's interval around July 03, and COSIMA was hit by one particle that fragmented on the target. Given that the total collection areas of GIADA and COSIMA differ by a factor of 30, the total numbers of detected particles are consistent, and the COSIMA particle stems with high probability from the outburst.

If we sum the volumes of all the fragments on the COSIMA targets, assuming they have a half-sphere shape, accounting for some flattening upon impact, we obtain a total volume of 2.3×10^{-12} m^3. This volume corresponds to a spherical particle of about 160 μm in diameter. As fragments from the parent impacting particle may have stuck to the dust funnel's walls, the particle size stated is a lower limit estimate.

The size distribution of the fragments of the collected particle gives a hint on the tensile strength and/or the velocity of the incoming particle. A very fragile or very fast particle would tend to
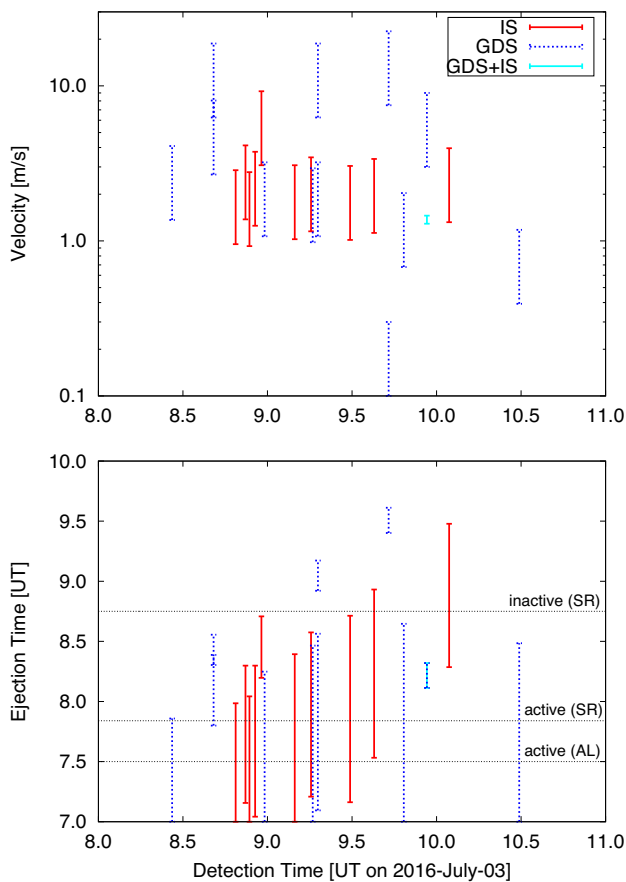
Figure 6. Velocities (top panel) and inferred starting times (bottom panel) of particles detected by GIADA. The velocities of the IS-only particles were determined using the method described in Della Corte et al. ([2016](#)) using a value for the reference speed, A, optimized for this particular event such that all IS-only particles are compatible with ejection during the time interval confined by the first detection of activity by Alice and the observation of the inactive surface by OSIRIS. The error bars correspond to a velocity uncertainty of 50 per cent for the IS-only and GDS-only detections.

break into a lot of small fragments, whereas a low velocity and/or strongly bounded aggregate would tend to break into few big pieces. The cumulative power index of the size distribution shown in Fig. [8](#) is −2.54. This power index is very close to the average power index of −2.3 ± 0.2 measured for the size distribution of fragments of particles collected before perihelion at heliocentric distances ranging from 3.57 to 2.36 au (Hornung et al. [2016](#)). This implies that the particle tensile strength is of the same order of magnitude than previously reported values of several hundreds of Pa. Then the velocity would range from 2 to $5\,\mathrm{m\,s^{-1}}$, and the particle density would be $200\text{–}300\,\mathrm{kg\,m^{-3}}$ (Hornung et al. [2016](#)). This density range implies that the estimated mass of the particle collected during this week is $(0.5\text{–}0.8) \times 10^{-9}\,\mathrm{kg}$. With an assumed density of $1000\,\mathrm{kg\,m^{-3}}$, the total mass would be higher, $2.3 \times 10^{-9}\,\mathrm{kg}$, and would imply a higher tensile strength and higher velocity of the impacting particle (Hornung et al. [2016](#); Merouane et al. [2016](#)).

2.5 STR-B

The *Rosetta* spacecraft carried two identical Star Trackers (STR-A and STR-B) as part of its attitude control system (Buemi, Landi & Procopio [2000](#)). The STR cameras had apertures of 29 mm, an effective focal length of 46 mm, and a FOV of $16.4° \times 16.4°$. They

were equipped with CCD detectors comprising 1024×1024 pixels, and their sensitivity extended over a broad range in the visible spectrum.

In the nominal tracking mode, the instrument continuously measured the position and magnitude of up to nine stars in the FOV in order to derive the spacecraft attitude. In this process, the background signal was determined in 20×20 pixel windows containing the tracked stars. The average of this quantity over all tracking windows is available as a housekeeping parameter downlinked with a typical sampling interval of 32 s. The parameter value was then bias-corrected and converted into spectral radiance units based on information extracted from the magnitude calibration relations applied by the instrument for stellar targets.

During the time of the outburst, STR-B was continuously obtaining data, measuring the average surface brightness, I_{STR} in its FOV. Mounted on the spacecraft with a boresight offset by 100° from that of the science instruments and pointing away from the main outburst site, the STR-B would have detected dust from the outburst only when it arrived close to the spacecraft, such that it can be directly set in relation to the measurements by the *in situ* instruments. Fig. [9](#) shows the temporal profile of the surface brightness measured by the STR-B. The peak flux was observed at UT 08:50, about simultaneously with GIADA. This suggests that the dominant optical cross-section of dust released during the outburst was in particles in the sensitivity range of GIADA, a few $100\,\mu\mathrm{m}$ in radius.

3 RESULTS

3.1 Dust velocity

Assuming that the outburst started between 7:30 (first illumination) and 7:36 (first Alice detection), the fastest particles, detected by the STR-B at 07:40, travelled at a speed of $(25 \pm 10)\,\mathrm{m\,s^{-1}}$. Particles seen by STR-B at 14:00 and having started from the comet after 7:30 and having left the OSIRIS FOV by 8:48 had a velocity of $(0.41 \pm 0.05)\,\mathrm{m\,s^{-1}}$.

3.2 Outburst duration and timing

Assuming that the outburst did not start before the site was exposed to sunlight at 7:30 and that the slowest particles ($0.41\,\mathrm{m\,s^{-1}}$) would have needed 10 min to leave the OSIRIS FOV (250 pixel distance) by 8:48, we limit the duration of the outburst to a maximum of 68 min.

If the outburst had been an instantaneous event, it would need to have occurred not later than at 7:36. In that case, even the slowest known particles travelling at $0.41\,\mathrm{m\,s^{-1}}$ would have been at 350 m distance from the outburst site at 7:50, and all particles visible in the OSIRIS image would have been slower than those detected by STR-B at 14:00. In that case, Alice would have observed much faster particles than OSIRIS, likely those creating the *in situ* detection peak between 8:30 and 9:00, and – based on the STR-B measurement – the surface brightness measured by Alice should have been a factor of 10 higher than that measured by OSIRIS, which is in contrast to the observed value of 0.25 (Section 3.3). We therefore exclude an instantaneous event and assume that the activity was still on-going at 7:50, giving a minimum duration of 14 min.

3.3 Plume surface brightness and shadow

To evaluate the amount of light (1) scattered by dust in the plume towards the camera and (2) prevented from reaching the surface,
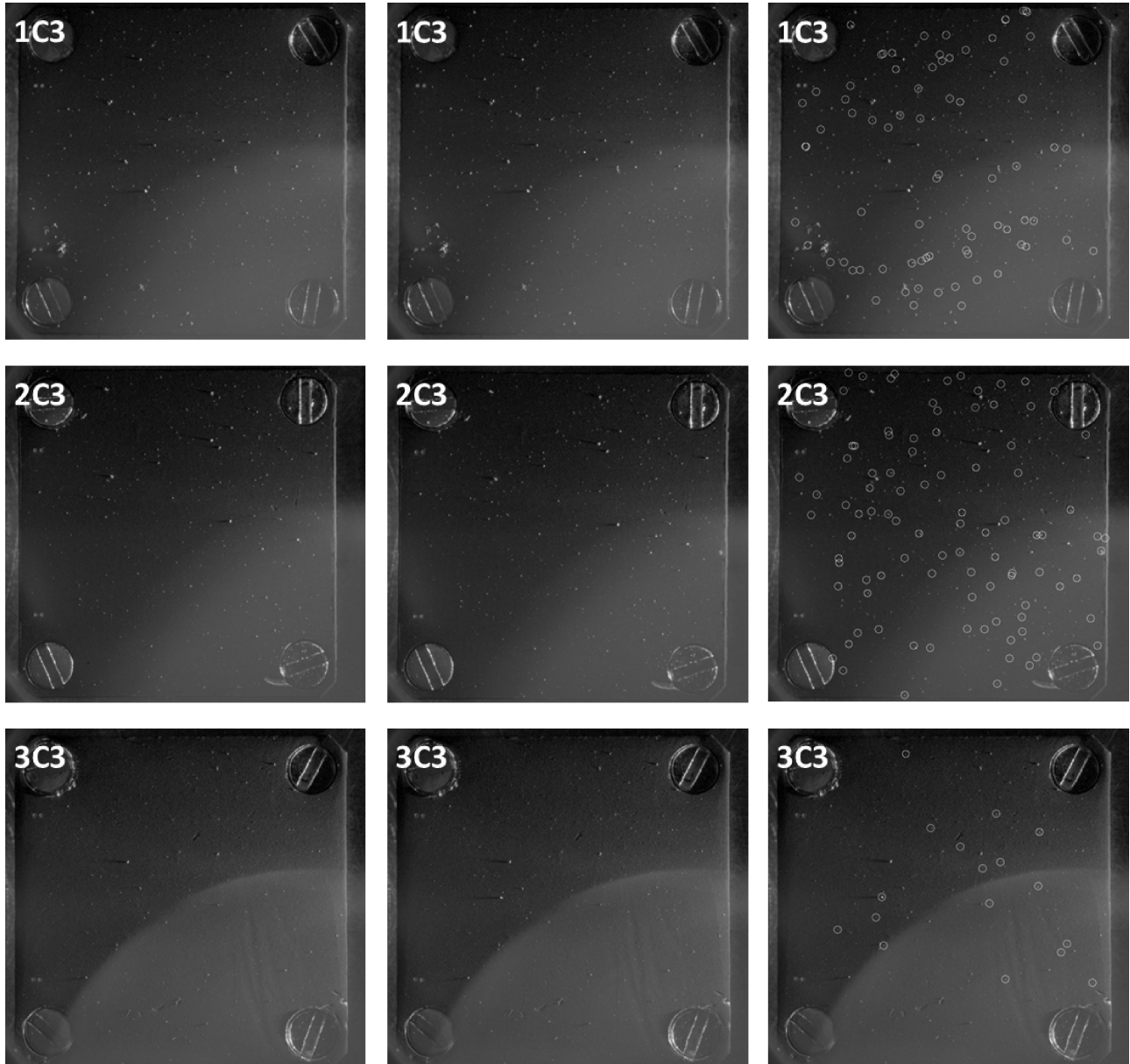
Figure 7. COSISCOPE optical microscope images of targets. Left column: before the exposure period of 2016 July 01–07. Centre column: after the exposure. Right column: with the locations of the particles that were collected during this period marked.

we use the NAC image of 2016 May 03 00:42 (Fig. 2, right) as a reference for the brightness of the surface in the absence of a plume. In both images, we measured the surface brightness in ∼3600 circular apertures having projected radii of 1.72 m. The positions of these apertures were manually selected to match the same landmarks such as boulders and their shadows in both images, resulting in ∼3600 pairwise measurements of the surface brightness, each pair consisting of one measurement on the outburst image, $I_{\mathrm{outburst}}^{j}$, and one on the reference image, I_{ref}^{j}, were j identifies the pair. The surface brightness measured on the reference image was scaled by a factor of $f = 0.842$ to account for the different heliocentric distance and central wavelength. For each pair, we calculated the ratio $R = I_{\mathrm{outburst}}/(fI_{\mathrm{ref}})$ (colour-coded in Fig. 10) and the difference $I_{\mathrm{plume}} = I_{\mathrm{outburst}} - fI_{\mathrm{ref}}$ (grey-scale in Fig. 10), and averaged over all pairs within 20×20 pixel squares of the outburst image. To calculate the average value of R in a square, we considered

only illuminated spots on the surface. The ratio R characterizes the depth of the shadow and is meaningful in the predominantly shadowed region of the surface. The difference, I_{plume}, corresponds to the amount of light scattered by dust in the plume. In the central region of the plume, no contours of the underlying cometary surface could be identified even at highest possible stretching of the brightness scale. We interpret this as an optically thick region of the plume and assume that all light received was scattered or absorbed by dust. The shadowed region closest to the plume origin [around coordinates (900,500) in Fig. 10] is seen through a considerable amount of foreground plume dust that increases the value of R. In general, the innermost region of the plume ($860 < x < 920$, $500 < y < 600$) seems to be characterized by a complex interplay of light scattering by the dust and by the surface and shadowing by the dust. An interpretation of this region would require a detailed model of the dust distribution and light scattering and is beyond the scope of

Table 4. Numbers of particles collected by COSIMA during the period between 2016 June 06 and July 19. Between June 08 and July 01, no target was exposed. The first two columns list the start and end date (in 2016) of the exposure period. N_f is the number of individual particle fragments identified on the target, and N_p is the number of parent particles from which these fragments have been inferred to derive from. The quantity N_p is assumed to be 1 if the spatial distribution of the particles collected during the exposure period of interest is not random. The method to determine N_p is described in Merouane et al. (2016). The volume, V, is calculated by deriving the radius of the particles on the target, assuming a circular shape and calculating the volume of a half sphere (to take into account a flattening of the particles after impact on the target).

T_{start} (UT)	T_{end} (UT)	N_f	N_p	V (m³)
Jun-06 03:04:19	Jun-06 06:40:13	0	0	0
Jun-06 08:24:45	Jun-07 13:15:14	0	0	0
Jun-07 14:55:26	Jun-08 00:00:11	1	1	8.3×10^{-15}
Jul-01 12:52:09	Jul-07 07:13:45	188	1	2.3×10^{-12}
Jul-07 10:40:55	Jul-13 05:55:10	19	1	1.5×10^{-12}
Jul-13 09:22:12	Jul-16 20:41:30	11	1	1.4×10^{-13}
Jul-17 00:08:54	Jul-19 19:03:37	5	5	3.8×10^{-13}

Figure 9. Surface brightness in the FOV of the STR-B as a function of time.

Figure 10. The outburst image subtracted (grey-scale) or divided (colour) by the May 03 image scaled to account for the different heliocentric distances and filter bands. The grey-scale represents the surface brightness of light scattered by dust in the plume, while the colour code indicates the fraction of light prevented from reaching the surface by the dust. In the central region (framed in green), the surface brightness is given as on July 03, assuming that the dust column was optically thick. Each square has a projected linear size of 17.2 m at the distance of the comet. The numbered fields were used to derive the dust albedo in Section 3.5 from the extinction of light reaching the surface (white fields) and the surface brightness of light scattered by dust in the plume (red fields). The geometric association of the fields is based on the assumption that the darkest region of the shadow was cast by the brightest section of the plume.
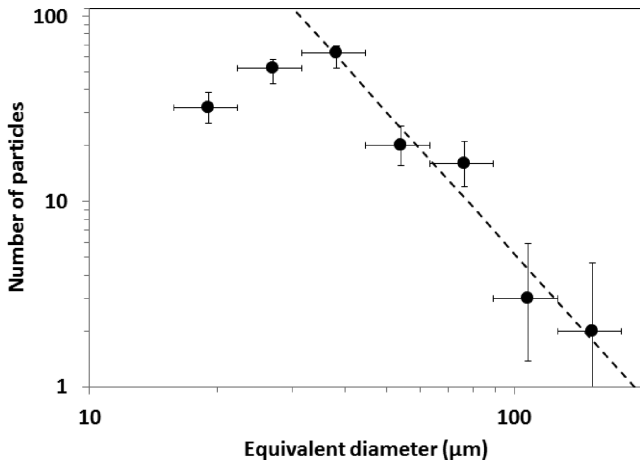

Figure 8. Size distribution of particle fragments collected on the COSIMA targets during the exposure period including the outburst. The cumulative power index is -2.54, which is close to the value measured for all the particles collected after perihelion (-2.58). However, since the particles from this outburst result from the fragmentation of a single parent broken in the funnel, the size distribution reflects that of the fragments. The measured power index should rather be compared to the value of -2.3 ± 0.2 measured for the size distribution of fragments of particles (Hornung et al. 2016). The method used to determine the number of particles and the error bars is described in Merouane et al. (2016).

this paper. It is possible that the lowest part of the plume appears relatively dark because it is shadowed by the dust above.

The typical plume surface brightness in the WAC red filter in the background-subtracted OSIRIS image is of the order of 4×10^{-4} W m^{-2} sr^{-1} nm^{-1}, corresponding to a radiance factor I/F of 8×10^{-3}. Alice measured a surface brightness of about 4000 rayleighs in the spectral range of 175–195 nm, corresponding to $I/F = 2 \times 10^{-3}$. Simultaneous measurements of OSIRIS and Alice on 2016 February 19 found a ratio of 2 between the OSIRIS- and Alice-measured radiance factors (Grün et al. 2016), as opposed to a factor of 4 in the present data. This slight difference is explained by the motion of the Alice slit during the 10 min integration, such that the central plume was covered by the slit only for about 30 per cent of the total integration time.
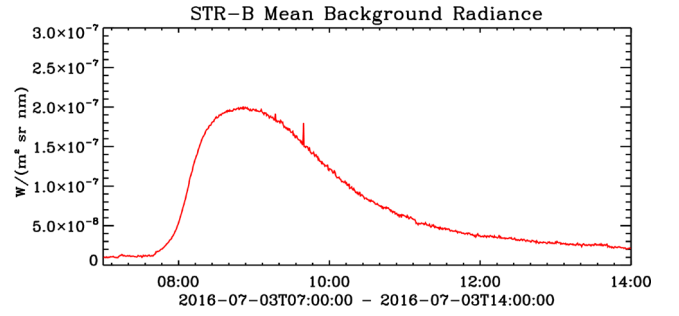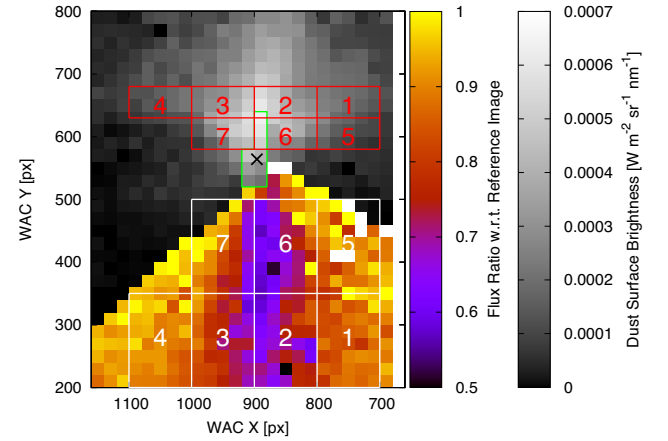
3.4 Plume orientation and shape

The plume in Fig. 2 has an opening angle of $(100 \pm 5)°$, possibly with a denser central region of $(25 \pm 5)°$ opening angle. Associating the brightest region in the plume P0 = (890,630) in Fig. 10 with the darkest part of the shadow S0 = (890,370), we calculate the three-dimensional point of intersection, *PI*, of the lines (a) connecting the point of intersection of S0 with the surface to the Sun, and (b) P0 to the spacecraft using the shape model SHAP5 v1.5 (Jorda et al. 2016) and the SPICE toolkit (Acton 1996). We define the footpoint of the plume, *PF*, from the intersection of the edges of the inner and outer cone, and calculate its three-dimensional position from the intersection of the line-of-sight crossing *PF* with the shape model. We interpret the line connecting *PF* and *PI* as the central axis of the cone. Had the plume originated from the centre of the comet reference frame, its direction would have corresponded to latitude $-41°$ and longitude 158° with an uncertainty of 10°, resulting from the size of the 20×20 pixel blocks used for the triangulation, and an

additional, difficult to quantify, uncertainty arising from the uncertainty of the pixel association. At 7:50, the line connecting *PF* to *Rosetta* was at an angle of $(35 \pm 10)°$ from the central plume axis. This angle increased over the following hours.

3.5 Dust albedo

We constrain the product of albedo and phase function at a phase angle of $95°$, P, of the plume material from the OSIRIS image in two ways. (1) Assuming that the innermost region of the plume was optically thick, we derive a lower limit of $P_{centre} = 0.012$. This is one order of magnitude brighter than the nucleus with $P_{nucleus} = 1.1 \times 10^{-3}$ (Fornasier et al. 2015).

In the second approach, we derive P from the cross-section of dust casting the shadow on the surface and the brightness of light scattered by dust. For each of the 20×20 squares shown at colourscale in Fig. 10, we calculated the projected area perpendicular to the solar direction $A_\perp$ and assumed that the total geometric cross-section of dust between the square, i, and the Sun was given by $C_i = (1 - R_i) A_\perp^i$, where R_i is the fraction of light removed from the incident flux in square i (Sec. 3.3). We then grouped the squares to seven larger fields of 100×150 pixels (white boxes in Fig. 10), and associated each of these fields with a complementary field in the coma (red boxes), again assuming that the darkest part of the shadow was caused by the brightest region of the plume (Section 3.4). We obtain for each pair of fields $j = [1,7]$ the total dust cross-section C_j in m^2 and the intensity of the scattered light I_j in $W\,m^{-2}\,nm^{-1}$, and calculate the product of geometric albedo and phase function, P_{plume}^j, from

$$P_{plume}^j = \frac{I_j}{C_j} \frac{\pi r_h^2 \Delta^2}{I_{sun}}, \tag{1}$$

where r_h is the heliocentric distance in au, Δ is the distance to the spacecraft in m, and $I_{sun} = 1.7\,W\,m^{-2}\,nm^{-1}$ is the solar flux at 1 au in the WAC/red bandpass. We find $P_{plume} = 0.025 \pm 0.002$, where the given uncertainty corresponds to the standard error of the mean from averaging over all seven fields. The similarity of values obtained for the different fields seems to support the chosen association of fields on the ground and on the plume. The measured value of P_{plume} is a factor of ~ 20 brighter than that of the nucleus. This factor is comparable to the ratio of a typical cometary dust phase function $\phi_{dust}(\alpha = 95°) = 0.5$ (Kolokolova et al. 2004), and the phase function of the nucleus $\phi_{nucl}(\alpha = 95°) = 0.02$ (Fornasier et al. 2015).

A possible interpretation is that the plume consisted of a mixture of dark refractory grains of several hundred micrometers having a nucleus-like albedo and phase function, and a component of bright ice grains as detected by Alice. The phase function of ice crystals depends strongly on their shape and texture. For $0.1 < P_{ice} < 0.2$ (Liu et al. 2006), an admixture of (12–25) per cent in cross-section of such bright grains would be required to raise the average by a factor of 20. Liu et al. (2006) model the geometric albedo of ice grains of various shapes as a function of the phase angle. At $\alpha = 95°$, they find $P_{ice} = 0.1$ for spheres and $P_{ice} = 0.2$ for a mix of cylinders, while the value for spheroids is between these extremes. Their computations were done for a size distribution of particles with the efficient particle radius of $5\,\mu m$ and at a wavelength of $1.88\,\mu m$. Since in light scattering the defining characteristic is the ratio of radius to wavelength, then 5/1.88 should give the same results as particles of radius $1.5\,\mu m$ at the wavelength $0.6\,\mu m$ used in our observation, which is slightly larger than the particle size derived by Alice. The imaginary part of the refractive index of ice is slightly larger at $1.88\,\mu m$ (10^{-4}) than at visible wavelengths (10^{-6}). But this difference in absorption is not significant enough to strongly affect the results.

3.6 Dust mass and production rate

The total dust cross-section ($C = \sum_i C_i$) causing the observable shadow is $6200\,m^2$. If (75–88) per cent of this cross-section were contributed by particles of a representative $250\,\mu m$ radius, the corresponding volume would be $(1.6–1.8)\,m^3$, or a disc of 10 m radius and (5–6) mm thickness. For a density in the range of $\rho = (250–795)\,kg\,m^{-3}$, the equivalent mass would be $M_{image} = (920 \pm 530)\,kg$. The main uncertainty of the mass estimate results from the uncertainty of the average density, the range of which we chose to include both the COSIMA value of $250\,kg\,m^{-3}$ (Sec. 2.4) and the GIADA average density of $795\,kg\,m^{-3}$ (Fulle et al. 2016). The mass M_{image} is a lower limit to the total ejected dust mass, because an unknown fraction of the dust was outside the FOV, and because the activity continued over a time interval between 14 and 68 min.

The extinction cross-section was measured on dust at a distance of 20–100 m from the source (Fig. 10). At these distances, the dust travels at (90–105) per cent of the terminal velocity (Jewitt et al. 2014). Assuming a representative dust velocity of $2\,m\,s^{-1}$ (Section 2.3), dust leaves the shadow-casting region of the plume in $\sim 50\,s$. This gives a dust production rate of $Q_M = (18.4 \pm 10.6)\,kg\,s^{-1}$ or a number flux of $Q_N = (5.1 \pm 0.4) \times 10^8\,s^{-1}$. For a duration of 14–68 min and assuming a constant production rate, the estimated total mass of ejected dust is between 6500 and 118000 kg. The excavated volume lies in the range of $(26–150)\,m^3$, corresponding to a layer of (8–47) cm for a 10-m radius patch (Section 3.8).

If the dust was distributed uniformly across a cone with an opening angle of $100°$ (solid angle of 2.24 sr), we expect a number flux of $F_{GD} = (0.0025 \pm 0.0002)\,s^{-1}$ on the $0.01\,m^2$ sensitive area of GIADA (subtending a solid angle of 1.1×10^{-11} sr as seen from the comet). This leads us to expect a detection of (23 ± 2) particles over a 2.5-h time period in good agreement with the 22 actually detected particles.

3.7 Dust size distribution

In the following, we derive the dust size distribution from the combined measurements of STR-B and GIADA. If the outburst had been of negligible duration, we could associate a single particle size passing by the spacecraft to any given time. Assuming that the relative distribution of the spatial dust density along the STR-B line of sight and the dust optical properties did not change with time, then $(I_{STR} - I_{bg})/s^2$ reflects the relative number of particles of size $s(t)$ in the FOV, where $I_{bg} = 10^{-8}\,W\,m^{-2}\,nm^{-1}\,sr^{-1}$ is the pre-outburst background level, and $t = t_{obs} - t_{start}$ is the time required by the particle leaving the comet at t_{start} to cover the distance $D = 8500\,m$ from the outburst site to the spacecraft, and $v(t) = D/t$. Following Wallis (1982), we assume a unique relation $s \propto v^{-2}$, between particle size, s, and velocity, v, and hence $s(t) = s_0 \sqrt{t/t_0}$, with $s_0 = 200\,\mu m$ and t_0 the difference between UT 08:50 and t_{start}, for which we use a range of fixed values covering the possible duration of the outburst. The surface brightness I_{STR} is proportional to the number of particles in the FOV, N and their squared radius s^2. For a power-law differential size distribution,
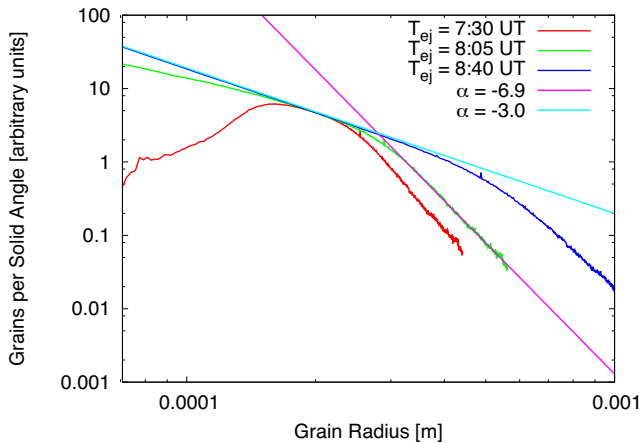
$$\frac{dn}{ds} = s^\alpha, \tag{2}$$

Figure 11. Relative number of particles in the FOV $N = I_{STR}/s^2$ plotted versus $s = s_0\sqrt{t/t_0}$ for three different values of the starting time t_{start}. The data follow power laws of different exponents for 150 µm $< s < s_t$ and for $s > s_t$. For $s < 150$ µm (fast particles), the error introduced by the unknown starting time is too large to infer the dust size distribution, while this uncertainty only moderately affects the transition size (230 µm $< s_t < 500$ µm) and not the exponents.

follows $N(s) \propto s^{\alpha+1}$. Fitting a broken power law to the surface brightness as a function of time, we derive the exponents of the differential dust size distribution in Fig. 11. We find a significant change in the exponent, α, of the size distribution at a transition size, s_t, between 230 and 500 µm, depending on the assumed starting time. The exponent changes from $\alpha = -3.0$ for 150 µm $< s < s_t$ to $\alpha = -6.9$ for $s > s_t$. The transition size range dominates the optical cross-section of the dust.

3.8 Outburst site and surface change

OSIRIS observed the outburst site in the Imhotep Basin F multiple times during the mission. We here analyze a set of images obtained between January and August of 2016 to characterize the terrain at the outburst site. Selection criteria to assemble the data set included resolution and viewing geometry (Table 2). Some observations consist of multiple exposures in different bandpasses obtained within a short time interval, characterizing the spectral properties of the light scattered by the surface. The plume originated from a 20-m-diameter, roundish depression (D1) bounded to the southwest by a steep wall R of a few metres height and ~20 m length, to the north-east by a row of larger boulders (B1) and to the south-east by a single large and roundish boulder B2 (Figs 2 and 12).

The best images we found of the face of the wall R were obtained on 2016 March 19 with NAC at a resolution of 20 cm per pixel and lossless compression (Fig. 12, left-hand panel). The wall is in shadow, but indirectly illuminated by the surrounding sunlit surface. Its face shows some indications of thermal fracturing similar to that seen on the neighbouring boulders B1 and B2. It is possible that R is overhanging. In that case, the floor below would receive even less sunlight than the wall itself. The dark shadow at the foot of R could hide a crack.

The images constituting the right-hand panel of Fig. 12 were obtained 10 h before the outburst. The floor of D1 and of the neighbouring depression D2 shows patches of a bluish colour, indicating the presence of water ice (Pommerol et al. 2015; Barucci et al. 2016; Fornasier et al. 2016; Oklay et al. 2016). Since the July 02 observation was obtained at 14:20 local time, and the region emerged from

shadow at 10:17 local time, the face of the wall R was illuminated for not more than 4 local hours per rotation in July 2016.

On July 24, NAC images show a bright, bluish patch at the outburst site of a projected size of 15×5 m^2 (Fig. 13). The bright patch is also visible in images obtained under similar circumstances on July 09 and August 21 (Fig A3). An image of May 02 (12:59) that was also obtained under similar viewing conditions does not show the bright patch. Comparison of surface features in the May 02 and July 24 images shows that the terrain has not been altered outside a region between the bright patch and the boulder row B1, limiting the size of the affected area to a radius of ~10 m.

The visible bright patch is bounded towards the side of B1 by a shadow that gives the impression of a deep crack. To the opposite side, the bright surface makes an abrupt transition to terrain of more typical colour and brightness. The bright patch shows intrinsic brightness variations similar to those of the adjacent surface, which may indicate a similar, boulder dominated terrain. An apparent continuity of the light-shadow pattern between the bright and the typical terrain (marked by the arrow in the bottom panels of Fig. 13) may suggest that the bright material is a sharply bounded ice coating on the bouldered surface. Alternatively, the bright material could be a freshly excavated stretch of sub-surface material, and the sharp transition to the typical terrain could be a topographic feature such as the upper edge of a cliff.

Fig. 14 shows the relative reflectance of selected regions of interests (ROIs), normalized at a wavelength of 535 nm using a linear interpolation between 480 and 649 nm when the observations were not acquired in the green filter centred at 535 nm. Three of the selected ROIs are at the location of the bright patch, and three are on the adjacent terrain. The ROIs in the 24 July bright patch clearly show a much lower spectral slope than the surroundings, indicating exposure of some water ice (Barucci et al. 2016; Fornasier et al. 2016).

The bright patch at the outburst site was observable for at least 7 weeks. There are no suitable observations after August 21 to judge on its presence. From the observations of July 02 and 09, we constrain the diurnal duration of solar illumination of the icy spot to 1.18–3.11 local hours, corresponding to 0.59–1.56 h on Earth. An ice surface in vacuum at the temperature T sublimates at the rate of

$$Q_{H_2O} = p_{subl}(T)\sqrt{\frac{m_{H_2O}}{2\pi k_B T}}, \qquad (3)$$

where m_{H_2O} is the molecular mass of water, Q_{H_2O} is in kg s^{-1} m^{-2} and the sublimation pressure is given by $p_{subl}(T) = A\exp(-B/T)$ with $A = 3.56 \times 10^{12}$ Pa and $B = 6141$ K (Fanale & Salvail 1984). We calculate the temperature from the balance of radiative heating and cooling and sublimation cooling:

$$\frac{L}{N_A m_{H_2O}} Q_{H_2O} + \epsilon \sigma T^4 = (1 - A_B)\frac{I_\odot}{r_h^2}\cos\theta + I_{indirect}, \qquad (4)$$

where ϵ and A_B are the emissivity and Bond albedo of the surface, σ and N_A are the Stefan-Boltzmann and Avogadro constants, $L = 51\,000$ J mol^{-1} is the latent heat of water ice, θ is the angle between the surface normal and the solar direction, and $I_{indirect}$ represents illumination by scattered light and thermal radiation from other parts of the surface. We approximate this indirect illumination by the expression

$$I_{indirect} = \left[\frac{I_\odot}{r_h^2}A_B + \epsilon \sigma T_{extern}^4\right] f_{sky}, \qquad (5)$$

where f_{sky} is the fraction of sky of the primary surface occupied by other parts of the surface having the temperature T_{ext}.
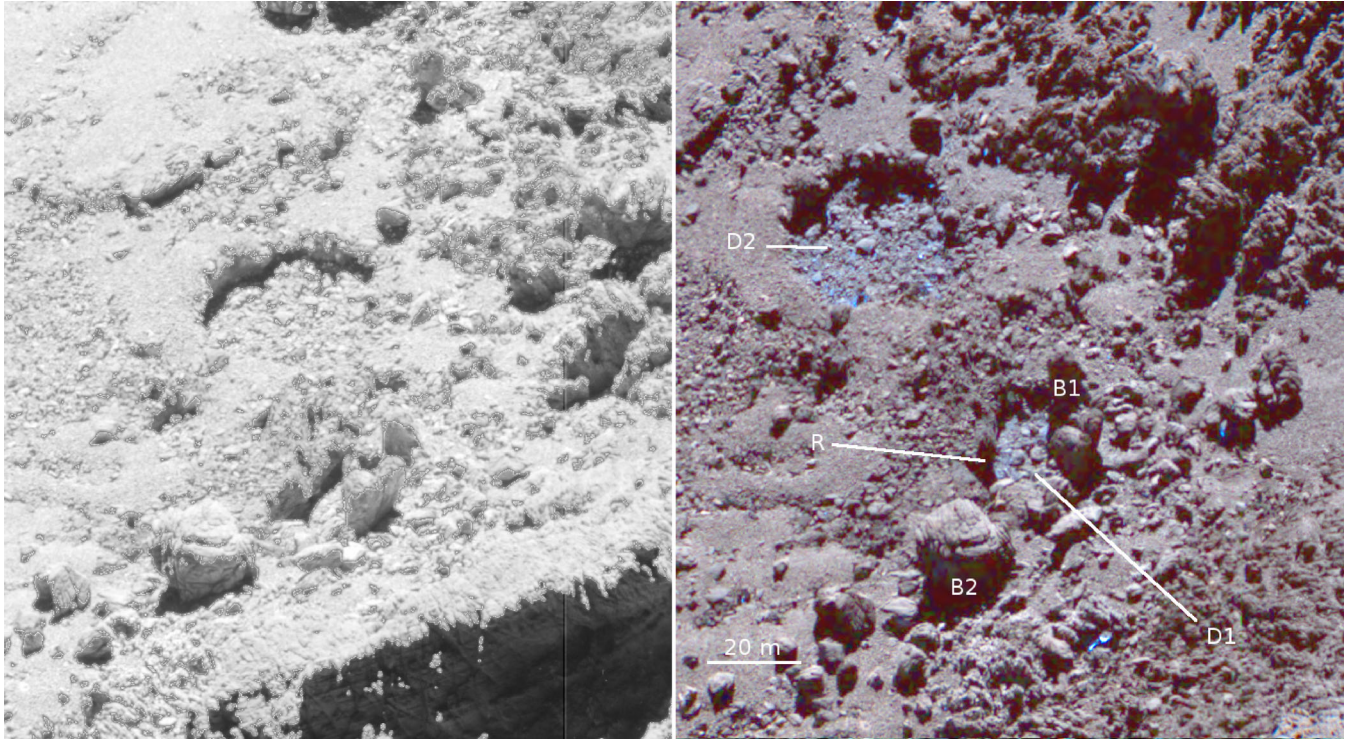
Figure 12. The outburst site on 2016 March 19 (left) and July 02 (right). The left-hand panel has two brightness scales: illuminated areas are shown at a logarithmic scale between 0 and 0.001 W m^{-2} nm^{-1} sr^{-1}, while a linear scale between 0 and 4×10^{-5} W m^{-2} nm^{-1} sr^{-1} is employed for areas hidden from direct sunlight but indirectly illuminated by the surrounding bright surface. The right-hand panel is a false-colour rgb composite with the red, green and blue channels corresponding to the NIR, orange and blue filters. The labels in the right-hand panel indicate the roundish depressions D1 at the foot of the plume of 2016 July 03, and D2, close to which a plume was observed on 2016 January 06. The wall R is located where after the outburst a bright blue patch was observed (Fig. 13), and the boulders B1 and B2 are indicated for orientation.

For the emissivity, we consider a range between 1 (correspond-ing to a blackbody) and an extreme of 0.6, consistent with excess temperatures of material in the debris trail (Sykes & Walker 1992). The average Bond albedo of the 67P surface in the green filter is $A_B = 0.012$ (Fornasier et al. 2015), and we use $A_B = 0.24$ measured on the Occator bright spots on Ceres (Li et al. 2016) as an upper limit for the bright icy patch.

Without indirect illumination, an ice surface having $A_B = 0.012$ and $\epsilon = 0.6$ illuminated at normal incidence at 3.32 au would have a temperature of $T_{\max} = 187$ K. For higher albedo and emissivity, and more shallow incidence, the temperature drops to $T_{\mathrm{low}} = 177$ K (cf. Table 5). Indirect illumination from a sky fraction of $f_{\mathrm{sky}} = 0.5$ and a dry and therefore hot (215 K) surface increases the temperatures by a few Kelvin. Sub-mm and mm-measurements by the MIRO instrument between 3.45 and 3.27 au in-bound do not show evidence for near-surface temperatures above 180 K (Schloerb et al. 2015). Sublimation rates corresponding to the above temperature range lie between 4×10^{-6} and 4×10^{-5} kg s^{-1} m^{-2}. Assuming a bulk density of 500 kg m^{-3}, and an illumination duration of 0.59–1.56 h per 12.055-h rotation, we expect that the ice layer eroded by 0.8–28 mm during 7 weeks, such that its initial thickness must have been at least 1 mm.

3.9 Frequency of outbursts

On 2016 January 06, a dust plume similar in shape to that seen on July 03 but a factor of 10 less bright was observed near D2. The plume appeared within 10 min from the time when the surface emerged from the shadow cast by the northeastern wall of basin F.

Comparison with a similar image obtained on 2016 May 03 shows that the location of the plume is consistent with the southwestern wall of D2 (Fig. 15). This suggests that the southwestern walls of circular depressions in the Imhotep Basin F may be preferred loca-tions for morning outbursts. However, the plume activity does not occur on every morning, because we saw each depression emerge from shadow without displaying a plume at least twice (D1: on 2016 May 03, 00:42, and on 2016 June 13, 17:20; D2: on 2016 May 03, 12:25, and on 2016 June 02, 16:56).

4 DISCUSSION

4.1 Free sublimation of an icy surface

The GIADA data show that a particle of 310 μm radius was acceler-ated to a terminal speed of 1.4 m s^{-1}. In the following, we examine if this velocity is consistent with the free sublimation of an icy surface.

The acceleration of dust from a small sublimating patch is de-scribed in Jewitt et al. (2014). From Table 5, we expect equilibrium temperatures between 177 and 189 K, and corresponding production rates between 1.4×10^{20} and 1.2×10^{21} s^{-1} m^{-2}. The surface tem-perature may drop significantly once the optically thick dust plume has formed (ranging from 165 to 180 K for $A_B = 0.012$, $0.6 < \epsilon < 1$ and $0° < \theta < 45°$, and a reduction of the solar irradiation to 50 per cent).

Assuming a gas speed of 600 m s^{-1} and an active patch of 10 m radius (Section 3.8), we plot the size–velocity relation from equation (A5) in Jewitt et al. (2014) for bulk densities of 250 and 800 kg m^{-3}
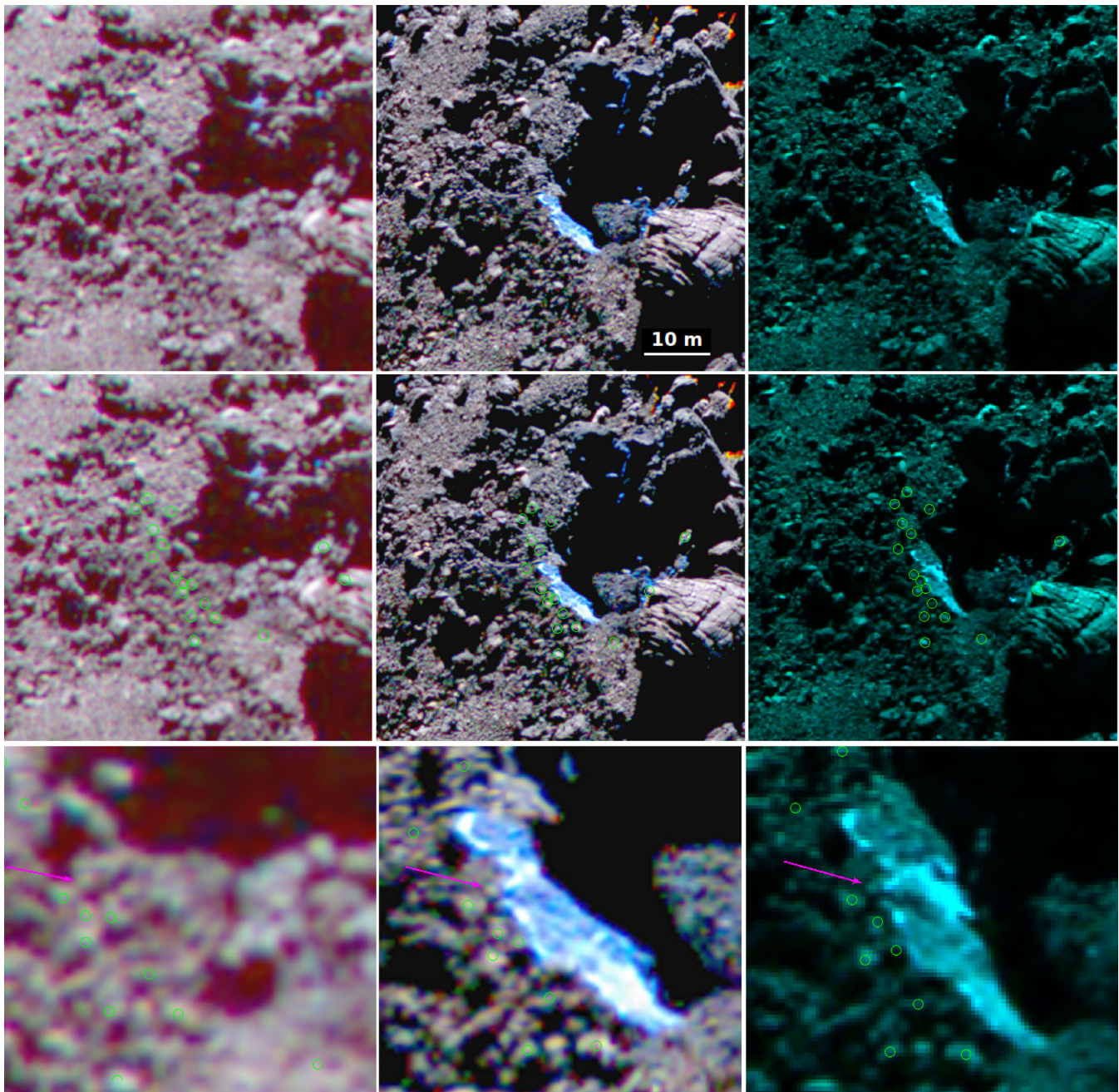
Figure 13. Left and centre columns: False colour rgb images of the outburst site, with different stretching levels, composed from OSIRIS/NAC images in NIR (red channel), orange (green channel) and blue (blue channel) filters. Right column: two-colour composite from orange (green channel) and blue (blue channel) filters, as no NIR data are available. The left column shows the image of May 02, the central and right columns show the images of July 24, 10:15 and 10:30, all at a similar spatial scale (cf. Fig. A3 in SM). In the central row, the positions of characteristic surface features are marked by green circles indicating the maximum extent of the region affected by the surface change. The bottom row shows a close-up of the bright patch, with the same green circles as above. The arrows point to a boulder row that seems to smoothly continue between the bright area and the surrounding darker area, and to have been in a similar position before and after the outburst. This may indicate that an ice layer froze out on top of the pre-existing surface.

and surface temperatures of 177 and 189 K in Fig. 16. For a density near the lower end and a temperature near the high end of the assumed intervals, the maximum liftable grain size is of order 1 mm and compatible with the GIADA and STR measurements. The dust velocities are therefore marginally consistent with a sublimating ice patch.

However, the derived dust production rate of $(18.4 \pm 10.6)\,\mathrm{kg\,s^{-1}}$ (Section 3.6) corresponds to $(0.06 \pm 0.03)\,\mathrm{kg\,s^{-1}\,m^{-2}}$ for a

10-m-radius patch, a factor of (1600 ± 800) higher than the highest gas production rate listed in Table 5. At such a high dust-to-gas mass ratio, the mass loading with dust would significantly influence the gas dynamics and reduce the velocity of both gas and dust. With a dust-to-gas velocity ratio of $\sim 1/200$, the dust at terminal velocity would carry only (4 ± 2) per cent of the initial kinetic energy of the gas, but $(8 \pm 4) \times$ its initial momentum, requiring a huge deceleration of the gas. It seems therefore highly unlikely that a
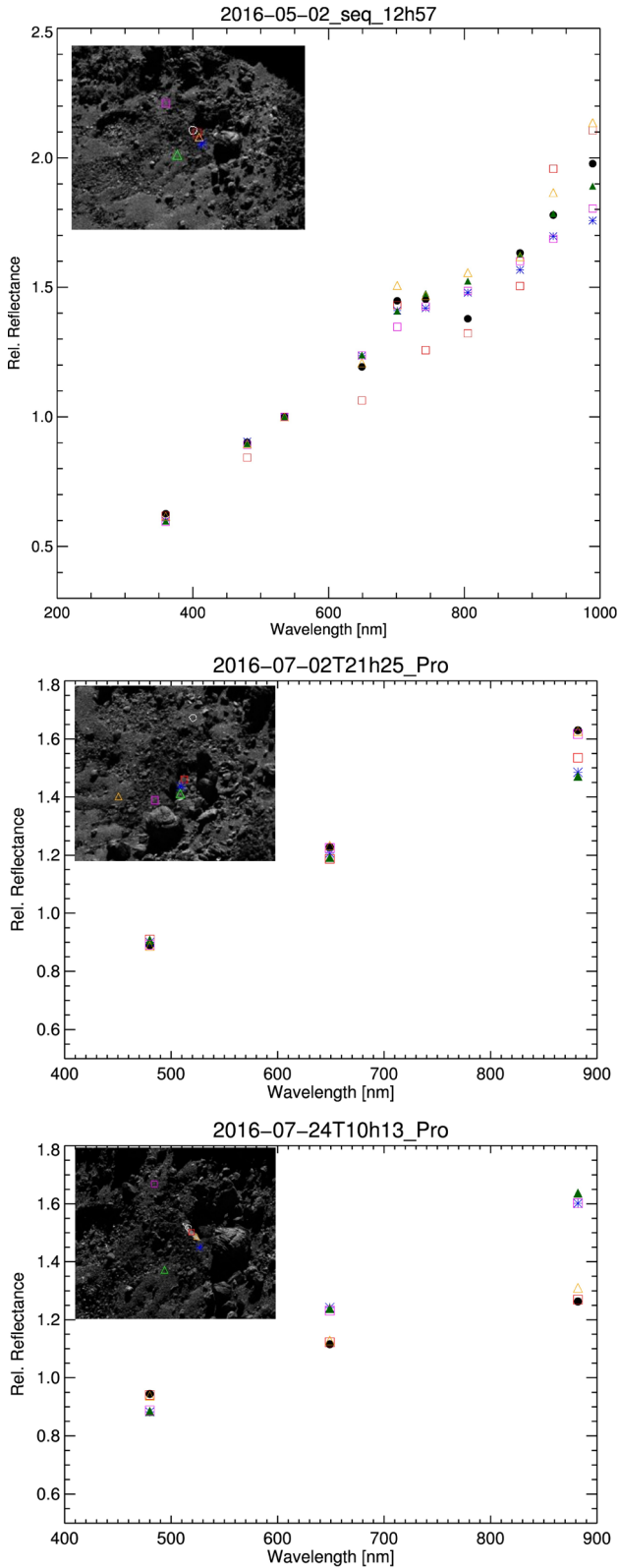
Figure 14. Spectral reflectance as a function of wavelength for the six ROIs following the method described in Fornasier et al. (2015, 2016). The bright patch on July 24 shows a strong blue colour (red square, black circle and orange triangle symbols).

freely sublimating surface of crystalline water ice can have caused the observed dust plume.

4.2 Outflow from a pressurized sub-surface reservoir

An alternative model to explain elevated gas production rates is a pressurized sub-surface reservoir that vents into vacuum through a small opening, such as a crack formed in response to thermal stress. The tensile strength of the surface layers of comet 67P is estimated to $P_t = 3$–150 Pa (Groussin et al. 2015; Vincent et al. 2015; Basilevsky et al. 2016), which gives an upper limit to the possible pressure inside the cavity.

The mass flow rate of gas from a container at pressure p_{in} and temperature T_{in} through a slit of width a and length l into vacuum is given in Sharipov & Kozac (2009) as

$$\dot{M} = \frac{W\sqrt{m}}{\sqrt{2\pi k_B}} \frac{p_{in}\,a\,l}{\sqrt{T_{in}}}, \tag{6}$$

where m is the molecular mass of the gas, W is a dimensionless parameter characteristic of the flow regime (we use $W = 1.5$ for a viscous flow) and k_B is Boltzmann's constant. Substituting p_{in} with the sublimation pressure $P_{subl}(T)$ (Fanale & Salvail 1984) and requiring a minimum total gas production rate of 7.9 kg s^{-1} (to match the minimum dust production rate), we require a temperature $T_{in} = 260$ K for $l = 20$ m and $a = 1$ m and water vapour, corresponding to an internal pressure of 200 Pa. This temperature is significantly higher than the equilibrium temperature derived in Table 5. For CO_2 gas, an internal pressure of 120 Pa at 180 K would be sufficient to provide the required gas mass flux, which is easily compatible with a sublimation pressure of $\sim$30 000 Pa.

Behind the crack, the gas density drops approximately twice as fast as the temperature (Sharipov & Kozac 2009), while the sublimation pressure drops exponentially with temperature. The gas immediately behind the crack therefore is in a supercooled state and is expected to freeze out, especially in the presence of condensation nuclei such as dust grains. This could explain the observation of micron-sized water ice particles by Alice.

Assuming that the reservoir is not significantly refilled during the duration of the outburst, that the temperature inside the cavity remains constant and that the gas inside the cavity can be described by the ideal gas law, the pressure inside the cavity and the mass flux though the crack drop exponentially with an e-folding time, τ, proportional to the volume of the cavity:

$$\tau = \left(\frac{2\pi m}{k_B T_{in}}\right)^{\frac{1}{2}} \frac{V}{W\,a\,l}. \tag{7}$$

For the production rate to drop to 1/1000 of its initial value (maximum liftable grain size of 1 μm) in 14–68 min, we require ($120 < \tau < 590$) s. For water at 250 K, a volume of $(5 - 24) \times 10^5$ m^3 is required, corresponding to a sphere of radius (49–84) m, or a half sphere of radius (62–105) m. For CO_2 at 180 K, the required volume would be a factor of 2 smaller. The crack would therefore have extended over a considerable fraction of the cavity.

We now estimate how the production rate from the outburst would compare to the overall background level, if CO_2 was the driving gas. Assuming a global CO_2 production rate of 10^{25} s^{-1} (Fougere et al. 2016), and assuming that this distributes homogeneously over the illuminated hemisphere, we expect a typical CO_2 flux of 6×10^{-10} kg s^{-1} m^{-2} at the position of the spacecraft ($\sim$10 km from the comet centre). For the outburst, we assume that the gas production rate should be comparable to the dust production rate, 18.4 kg s^{-1}, and that this gas would distribute homogeneously
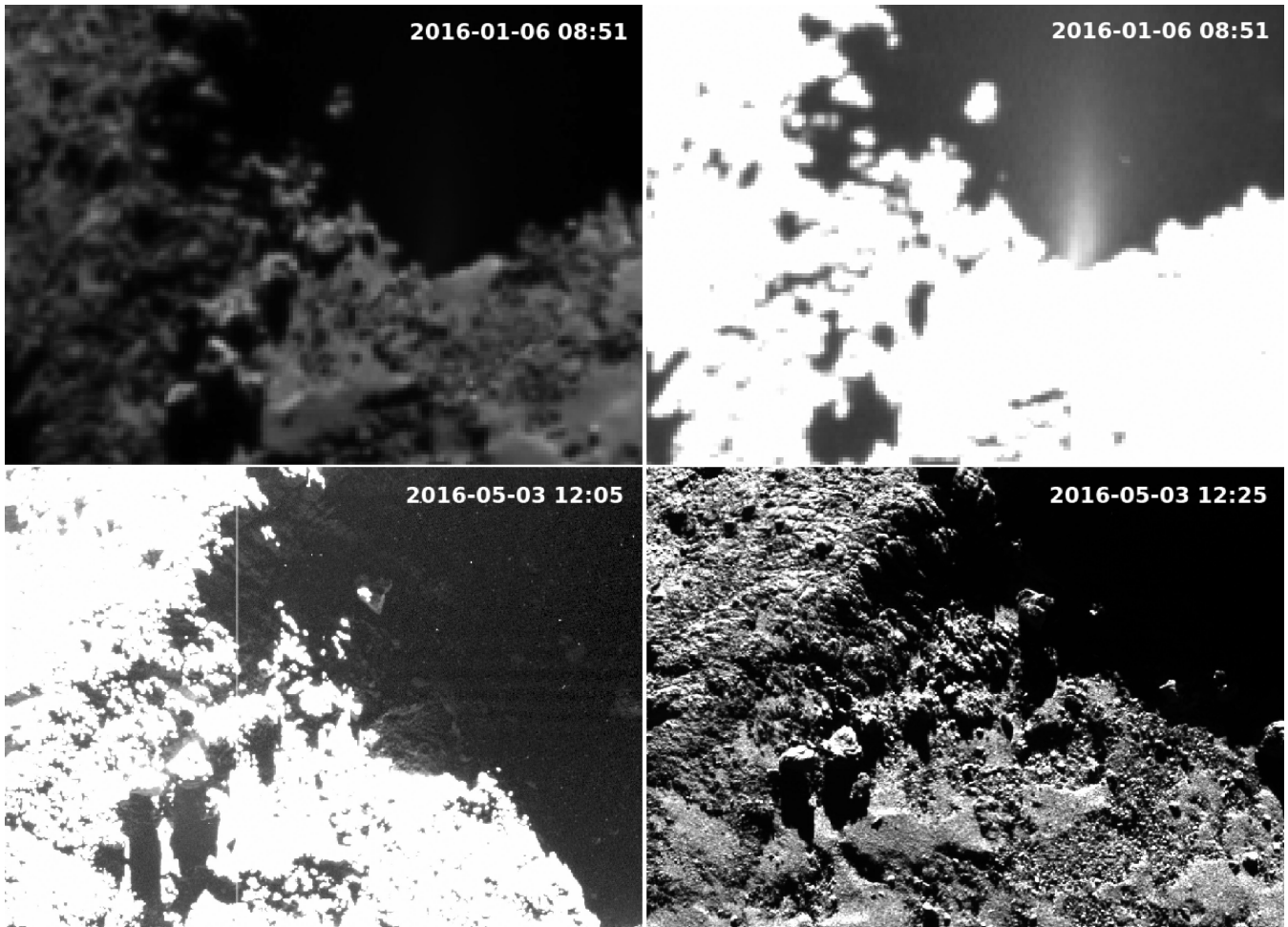
Figure 15. Basin F in Imhotep observed with NAC on 2016 January 06 and May 03. The two upper panels show the same image at different brightness scales. The left-hand panel is at a linear scale to show the topography, and the right-hand panel at a square-root scale to show the dust plume. The bottom panels show images of May 03 (left: square root scale, right: linear scale) for reference. In the left-hand panel, the circular depression is still in shadow, while in the right-hand panel, it is already exposed to sunlight. Comparison shows that the circular depression is the likely source region of the plume. The observation also shows that a dust plume does not occur at every sunrise.

over a half-sphere, such that at a distance of 8.5 km, the flux would be 4×10^{-8} kg s^{-1} m^{-2}, a factor of 68 above the estimated background. For CO, a similar calculation gives a factor of 110, if the global number production rate was comparable to that of CO_2.

If water vapour was the driving species, it must have been $\sim$80 K warmer than the surface equilibrium temperature. A possible energy source to heat water vapour could be the steady crystallization of amorphous ice in a deeper layer (González et al. 2008). It is possible that this process supplied a constant rate of sublimation and sufficient heat to build up a pressurized reservoir below a surface layer impenetrable for the vapour (Belton et al. 2008). Such a layer would need to have a thickness of centimetres to decimetres, and could consist of sintered material or of ice frozen out at a depth not reached by the diurnal heat wave. The accumulation of a sub-surface gas reservoir due to an internal heat source has been suggested by Belton et al. (2008). We here suggest a different trigger mechanism (thermal cracking) to explain the coincidence of the outburst with exposure to sunlight.

An alternative heating process could be the solid state greenhouse effect (Matson & Brown 1989), where heat is trapped below a surface composed of a visually translucent medium (such as ice or snow) that is opaque in the mid-IR and shows strong forward scattering (Hapke 1996). This effect can lead to a significant increase in temperature below the surface, although the magnitude and depth of the effect is strongly model dependent (Davidsson & Skorov 2002).

It is also possible that the sealed cavity was heated and filled with vapour around the time of perihelion, when solar irradiation was sufficient (Yelle, Soderblom & Jokipii 2004), and preserved both temperature and pressure due to a cover layer of low permeability and heat conductivity until it was opened by the crack formation. Future modelling work will have to investigate if the heating processes outlined above are consistent with the observed properties of the cometary surface and subsurface.

4.3 Transition from amorphous to hexagonal ice

Alternative to a pressurized gas bubble, we propose that amorphous ice may have been present behind the wall R and transformed to crystalline ice when, upon local sunrise on July 03, either a part of the overhanging wall collapsed or a newly formed thermal crack exposed it to solar irradiation. The temperature increase induced by the phase transition can have been sufficient to raise the sublimation
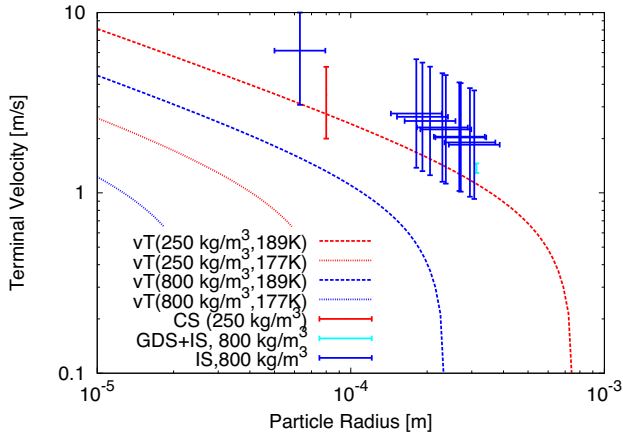
Figure 16. Terminal velocity as a function of particle radius derived from GIADA and COSIMA measurements, and expected maximum values v_T for an active patch of 10 m radius and gas speed of 600 m s^{-1} (Jewitt et al. 2014). The assumed bulk density is colour coded. Red: 250 kg m^{-3} (COSIMA = CS best estimate), blue: 800 kg m^{-3} (GIADA best estimate). The long dashed lines correspond to the maximum expected surface temperature of 187 K. The dotted lines correspond to the maximum temperature of 180 K measured by the MIRO instrument (Schloerb et al. 2015). The particle radii for GIADA data are derived from the measured momentum and the velocity assuming spheres of the indicated bulk density.

rate to a level consistent with the observed dust production rate and velocities.

At temperatures below $T_c = 200$ K and low pressure, ice freezing out from a vapour assumes the metastable crystal structure of cubic ice before transforming to the stable hexagonal ice, and below T_{as} = 160 K, amorphous ice can initially form (Murphy & Koop 2005). Since the face of the wall R was exposed to sunlight only for ~1/6 of a comet rotation and falls into shadow much earlier than the terrain bordering its top edge, it is possible that sublimation continued below the still illuminated surface and the vapour froze out behind the cold face of the wall. Since temperatures in the shadow fall easily below 160 K, this ice could be initially of cubic or even amorphous structure, as long as the deposition rate was sufficiently low for the substrate to absorb the considerable latent heat of condensation ($L \sim 51\,000$ J mol^{-1} = 2.83 × 10^6 J K^{-1}) without a significant rise in temperature.

It is beyond the scope of this paper to explore this possibility in due detail, such that we limit the discussion to simple energetic considerations. Assuming that the subsurface has a warmer (~100 K; De Sanctis et al. 2015) region below the surface illuminated during local afternoon, and a colder region behind the shortly illuminated wall, water vapour from the warmer subsurface could diffuse to the colder part and recondense there. The free sublimation rate of crystalline water ice at 100 K is 1.4 × 10^{-17} kg s^{-1} m^{-2}. This provides a condensation energy flux of 4 × 10^{-11} W m^{-2}. For the local increase in temperature not to exceed $\Delta T = 10$ K, and assuming that at a distance of $l = 4$ cm behind the condensation front the temperature is not elevated, we obtain a heat flux of $\dot{Q} = k \Delta T\, l = 2.5$ W m^{-2}, where k = 10^{-2} is the heat conductivity (Blum et al. 2017). The surrounding material may therefore be able to conduct the latent heat of condensation away from the condensation region without elevating the temperature to a point where amorphous ice could not exist. Even a significantly higher gas flux up to $\dot{Q}/L = 9 \times 10^{-7}$ kg s^{-1} m^{-2} (corresponding to $T = 170$ K) could be sustained, such that also vapour released in the immediate sub-surface could diffuse to the colder region and recondense there.

Table 5. Equilibrium temperatures of a sublimating ice surface at 3.32 au as a function of the Bond Albedo, A_B, the emissivity, ϵ, and the incidence angle of sunlight, θ, measured from the zenith. In all except the last line, no indirect illumination was considered. In the last line, it was assumed that the surface was additionally heated by scattered visible light and thermal radiation from nearby surfaces at 215 K covering 50 per cent of its sky.

A_B	ϵ	θ	T (K)	Q_{H_2O} (kg s^{-1} m^{-2})
0.012[a]	0.6[b]	0°	187	2.64 × 10^{-5}
0.012	0.6	45°	184	1.56 × 10^{-5}
0.012	1.0	0°	185	1.86 × 10^{-5}
0.012	1.0	45°	181	9.05 × 10^{-6}
0.24[c]	0.6	0°	185	1.86 × 10^{-5}
0.24	0.6	45°	182	1.09 × 10^{-5}
0.24	1.0	0°	182	1.09 × 10^{-5}
0.24	1.0	45°	177	4.25 × 10^{-6}
Measured (Ref. Schloerb et al. 2015)			180	3.76 × 10^{-6}
0.012	1.0	0°+	189	3.72 × 10^{-5}

[a]$A_B = 0.012$ was found for comet 67P (Fornasier et al. 2015); [b]$\epsilon = 0.6$ was derived for the debris trail of comet 67P (Sykes & Walker 1992); [c]$A_B = 0.24$ was found for Occator bright spots on Ceres (Li et al. 2016).

The metastable states transform to hexagonal ice on time-scales of minutes to days. The transformation can be accelerated by heating above T_c and T_{as} for cubic and amorphous ice, respectively (Murphy & Koop 2005). The transformations are exothermic. The latent heat of the transition from cubic to hexagonal ice is (110 ± 50) J mol^{-1}, and the heat capacity of hexagonal ice at 180 K is 26 J mol^{-1} K^{-1} (Murphy & Koop 2005), such that the transformation would lead to a temperature increase of (4 ± 2) K. The latent heat of the transition from amorphous to crystalline ice is of order 9 × 10^4 J kg^{-1} (González et al. 2008) or 1620 J mol^{-1}, corresponding to a temperature increase of 62 K following the phase transition in pure ice. Assuming that the freshly exposed surface had a radiative equilibrium temperature of ~180 K (Table 5), the temperature would have increased to ~240 K due to the crystallization. The corresponding sublimation rate would have been 0.033 kg s^{-1} m^{-2}, comparable to the inferred dust production rate of (0.06 ± 0.03) kg s^{-1} m^{-2}.

In order to sustain a gas production rate of 0.033 kg s^{-1} m^{-2} for at least 20 min, an ice mass of 40 kg is required. The face of the wall has an area of 20 × 10 m^2 (Fig. 12). For a condensation rate of 9 × 10^{-7} kg s^{-1} m^{-2}, the time required to build the crystallizing area is 3 days. For a condensation rate of 6 × 10^{-9} kg s^{-1} m^{-2}, the build-up time would be 1 yr, comparable to the duration of southern summer on 67P.

5 SUMMARY AND CONCLUSION

The described observations combine multifaceted measurements of the outflowing material with detailed information on the surface morphology and composition at the outburst site. Our key findings are:

(i) The outburst was located near a northeast-facing wall of ~10 m height in the Southern hemisphere.

(ii) The wall emerged from the shadow of a higher, opposite wall after the cometary night 6 min before the first detection of the outburst.

(iii) The surface at the foot of the wall was enriched in water ice before the outburst.

(iv) A similar dust plume was observed 6 months earlier to originate from a neighbouring depression with similar properties.

(v) The dust production was continuous, lasting at least 14 and not longer than 68 min.

(vi) The outburst altered a 10 m radius area of the surface and left an icy patch of a projected size of 15×5 m^2.

(vii) The ejected material comprised sub-micron-sized water ice grains at (12–25) per cent of the cross-section, and refractory dust several hundred micron in size.

(viii) The ejected dust mass was (6500–118 000) kg, corresponding to a layer of (8–47) cm for a 10m-radius patch.

(ix) The dust production rate was (18.4 ± 10.6) kg s^{-1}.

(x) For a freely sublimating water ice patch at 3.32 au, this would have corresponded to a dust-to-ice mass ratio of (1600 ± 800).

(xi) As such a high mass loading is inconsistent with the observed dust velocities, the free sublimation of water ice alone cannot explain the observed dust production.

(xii) We conclude that the release of energy stored in the subsurface must have supported the acceleration of dust.

The measurements of July 03 provide reasonably robust evidence that the event was driven by a process more vigorous than the free sublimation of ice and that some form of energy stored in the subsurface must have supported direct solar irradiation in accelerating dust. We have discussed two possible forms of such energy storage (a pressurized cavity and near-surface amorphous ice), but the viability of these propositions will have to be tested by future in-depth thermal models and comparison to a larger data set.

Auger et al. (2015) concluded from the radial pattern of fractures around Basin F, that it formed either by an impact or by the rising of a gas bubble. They interpret nearby roundish features as the walls of ancient gas conduits. It is therefore possible that there still is a gas-filled cavity below Basin F, and that the roundish features inside it are venting tubes still active.

Primordial amorphous ice has long been suspected to play a significant role in the evolution of the cometary interior and for outbursts (e.g. Prialnik, Benkhoff & Podolak 2004; Prialnik et al. 2008a). We here propose that ice recondensed from a vapour below a badly illuminated surface could initially be amorphous, too, and may cause violent outbursts when eventually exposed to sunlight.

However, Capria et al. (2017) find that primordial amorphous ice can exist as shallow as 1 m below the cometary surface, such that it is possible that the collapse of a 10 m high overhanging wall exposed such material.

Near-surface accelerations inconsistent with the free sublimation of water ice have been found in earlier studies (Agarwal et al. 2016; Kramer & Noack 2016), suggesting that the underlying process may be quite common and significantly contribute to the mass-loss in comet 67P.

REFERENCES

Acton C. H., 1996, PSS, 44, 65
Agarwal J. et al., 2016, MNRAS, 462, S78
Auger A.-T. et al., 2015, A&A, 583, A35
Barucci M. A. et al., 2016, A&A, 595, A102
Basilevsky A. T., Krasil'nikov S. S., Shiryaev A. A., Mall U., Keller H. U., Skorov Y. V., Mottola S., Hviid S. F., 2016, Sol. Syst. Res., 50, 225
Belton M. J. S., 2010, Icarus, 210, 881
Belton M. J. S., Feldman P. D., A'Hearn M. F., Carcich B., 2008, Icarus, 198, 189
Blum J. et al., 2017, MNRAS, in press
Buemi M., Landi A., Procopio D., 2000, in Schürmann B., ed., ESA SP-435, Spacecraft Guidance, Navigation and Control Systems. ESA, Noordwijk, p. 279
Capria M. et al., 2017, MNRAS, in press
Davidsson B. J. R., Skorov Y. V., 2002, Icarus, 159, 239
De Sanctis M. C. et al., 2015, Nature, 525, 500
Della Corte V. et al., 2014, J. Astron. Instrum., 3, 1350011
Della Corte V. et al., 2016, MNRAS, 462, S210
Fanale F. P., Salvail J. R., 1984, Icarus, 60, 476
Feaga L. M. et al., 2015, A&A, 583, A27
Feldman P. D. et al., 2015, A&A, 583, A8
Feldman P. D. et al., 2016, ApJ, 825, L8
Fornasier S. et al., 2015, A&A, 583, A30
Fornasier S. et al., 2016, Science, 354, 1566
Fougere N. et al., 2016, MNRAS, 462, S156
Fulle M. et al., 2015, ApJ, 802, L12
Fulle M. et al., 2016, MNRAS, 462, S132
González M., Gutiérrez P. J., Lara L. M., Rodrigo R., 2008, A&A, 486, 331
Groussin O. et al., 2015, A&A, 583, A32
Grün E. et al., 2016, MNRAS, 462, S220

Hapke B., 1996, JGR, 101, 16833

Hendrix A. R., Hansen C. J., 2008, Icarus, 193, 323

Hornung K. et al., 2016, PSS, 133, 63

Hughes D. W., 1990, QJRAS, 31, 69

Jewitt D., Ishiguro M., Weaver H., Agarwal J., Mutchler M., Larson S., 2014, AJ, 147, 117

Jorda L. et al., 2016, Icarus, 277, 257

Keller H. U. et al., 2007, Space Sci. Rev., 128, 433

Kissel J. et al., 2007, Space Sci. Rev., 128, 823

Knollenberg J. et al., 2016, A&A, 596, A89

Kolokolova L., Hanner M. S., Levasseur-Regourd A.-C., Gustafson B. Å. S., 2004, in Festou M. C., Keller H. U., Weaver H. A., eds, Comets II. Univ. Arizona Press, p. 577

Kramer T., Noack M., 2016, ApJ, 823, L11

Langevin Y. et al., 2016, Icarus, 271, 76

Li J.-Y. et al., 2016, ApJ, 817, L22

Liu L., Mishchenko M. I., Cairns B., Carlson B. E., Travis L. D., 2006, J. Quant. Spectrosc. Radiat. Transfer., 101, 488

Matson D. L., Brown R. H., 1989, Icarus, 77, 67

McClintock W. E., Rottman G. J., Woods T. N., 2005, Sol. Phys., 230, 225

Merouane S. et al., 2016, A&A, 596, A87

Murphy D. M., Koop T., 2005, Q. J. R. Meteorol. Soc., 131, 1539

Oklay N. et al., 2016, MNRAS, 462, S394

Pajola M. et al., 2017, Nature Astron., 1, 0092

Pommerol A. et al., 2015, A&A, 583, A25

Prialnik D., Benkhoff J., Podolak M., 2004, in Festou M. C., Keller H. U., Weaver H. A., eds, Comets II. Univ. Arizona Press, p. 359

Prialnik D., Sarid G., Rosenberg E. D., Merk R., 2008a, SSR, 138, 147

Prialnik D., A'Hearn M. F., Meech K. J., 2008b, MNRAS, 388, L20

Schloerb F. P. et al., 2015, A&A, 583, A29

Sharipov F., Kozac D. V., 2009, J. Vac. Sci. Technol. A, 27, 479

Sierks H. et al., 2015, Science, 347, aaa1044

Skorov Y. V., Rezac L., Hartogh P., Bazilevsky A. T., Keller H. U., 2016, A&A, 593, A76

Steckloff J. K., Graves K., Hirabayashi M., Melosh H. J., Richardson J. E., 2016, Icarus, 272, 60

Sykes M. V., Walker R. G., 1992, Icarus, 95, 180

Tubiana C. et al., 2015, A&A, 583, A46

Vincent J.-B. et al., 2015, Nature, 523, 63

Vincent J.-B. et al., 2016, MNRAS, 462, S184

Wallis M. K., 1982, in Wilkening L. L., ed., IAU Colloq. 61: COSPAR Information Bulletin, Vol. 1981. Elsevier Science B.V., p. 10

Yelle R. V., Soderblom L. A., Jokipii J. R., 2004, Icarus, 167, 30

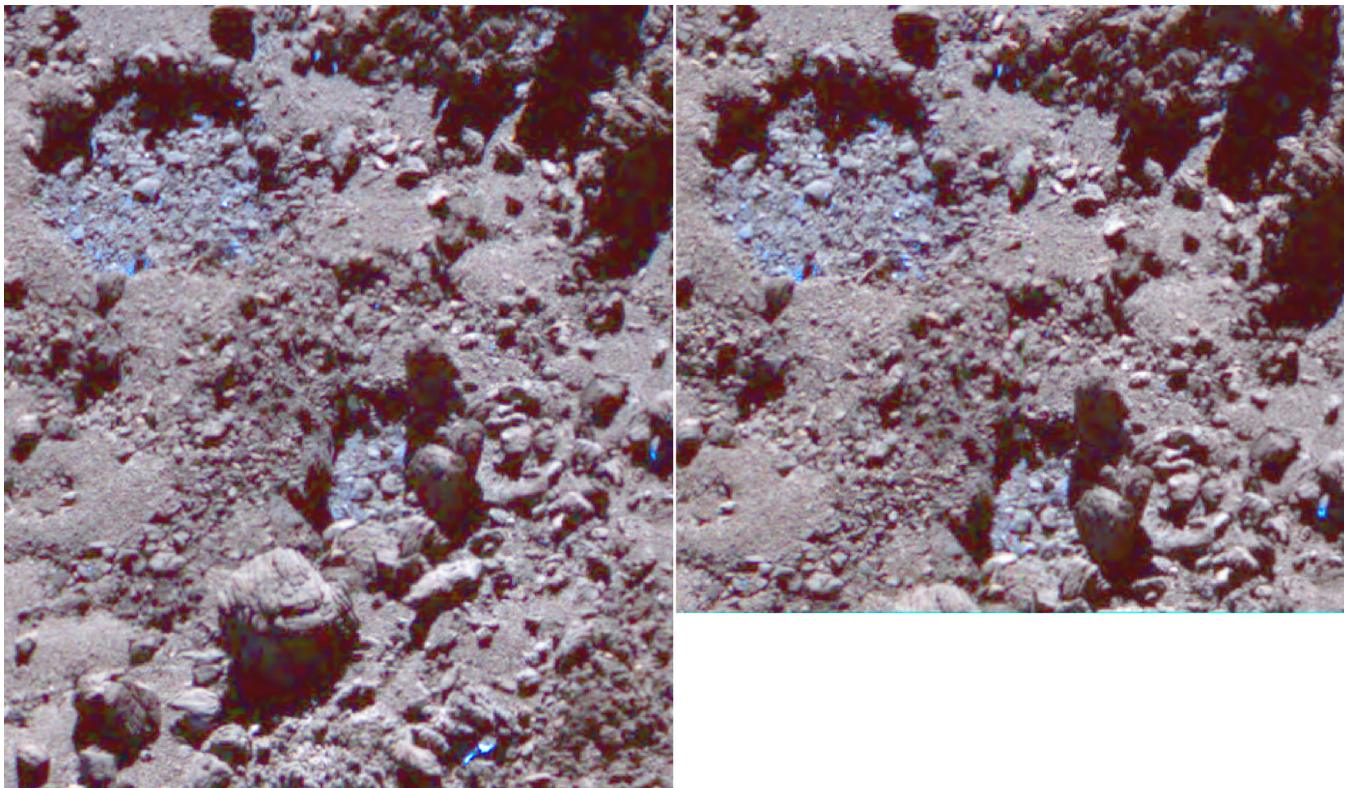## APPENDIX A: ADDITIONAL OSIRIS IMAGES

Figure A1. False colour rgb images composites of the outburst site on 2016 July 02, ∼10 h before the outburst, composed from three OSIRIS/NAC images in NIR (red channel), orange (green channel) and blue (blue channel) filters. The left-hand panel (identical to the right-hand panel in Fig. 12) shows observations obtained at 21:26, the right-hand panel is based on observations from 21:36.
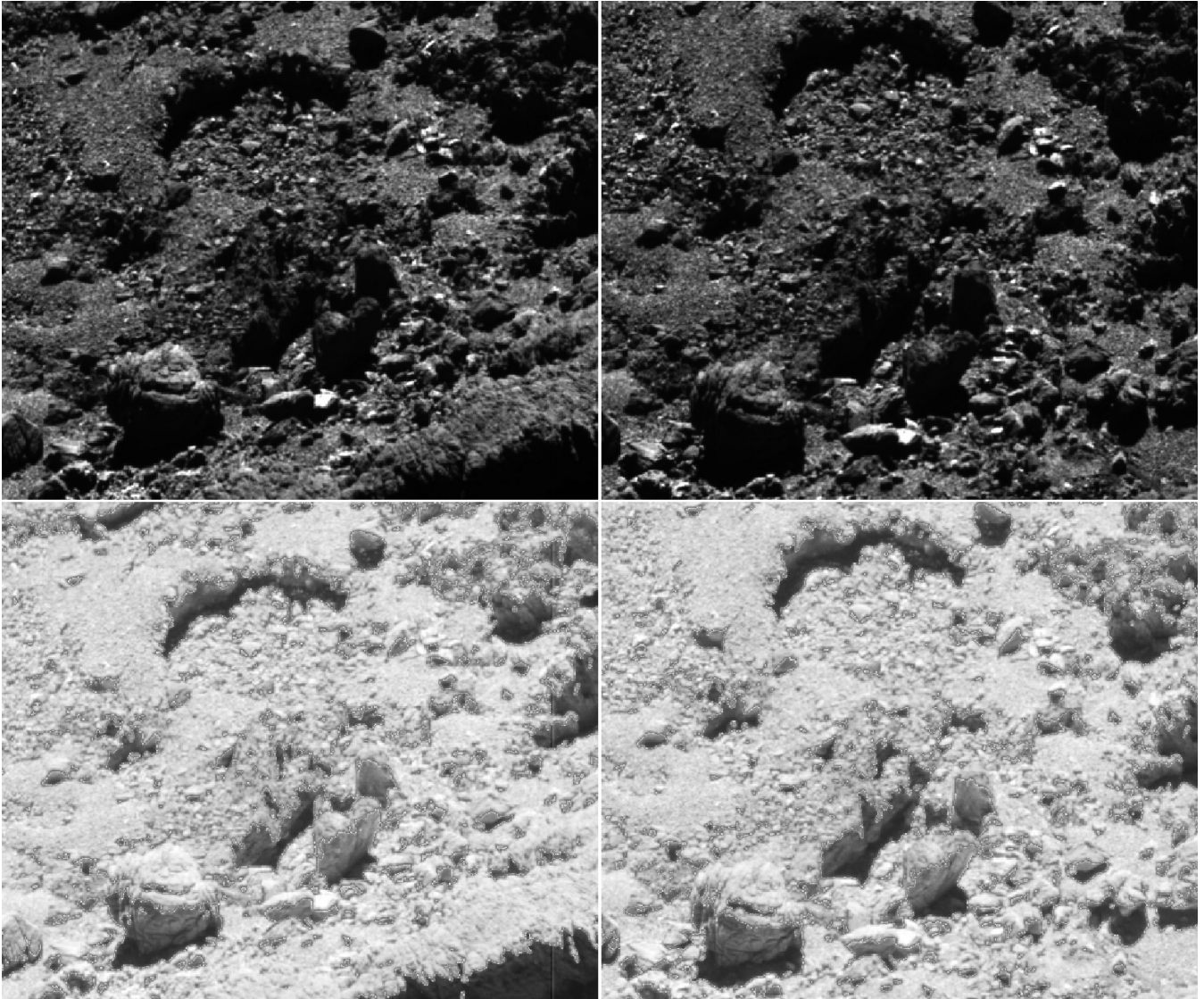
Figure A2. The outburst site D1 and the neighbouring depression D2 on 2016 March 19 at UT 21:26 (left) and 21:46 (right). The upper panels show the image at a linear scale ranging from 0 (black) to 10^{-4} W m^{-2} nm^{-1} sr^{-1}. The lower panels show the same images at a logarithmic scale between 0 and 10^{-3} W m^{-2} nm^{-1} sr^{-1} for illuminated regions and at linear scaling between 0 and 4×10^{-5} W m^{-2} nm^{-1} sr^{-1} for the shadowed regions to maximize visibility of the indirect illumination from the sunlit surface. These are to our knowledge the best images of the northeastern face of the wall R and its counterpart in D2. The projected size of the shadowed face of R is 17×7 m. These are lower limits due to the unknown angle of projection. The bottom left-hand panel is identical to the left-hand panel of Fig. 12.
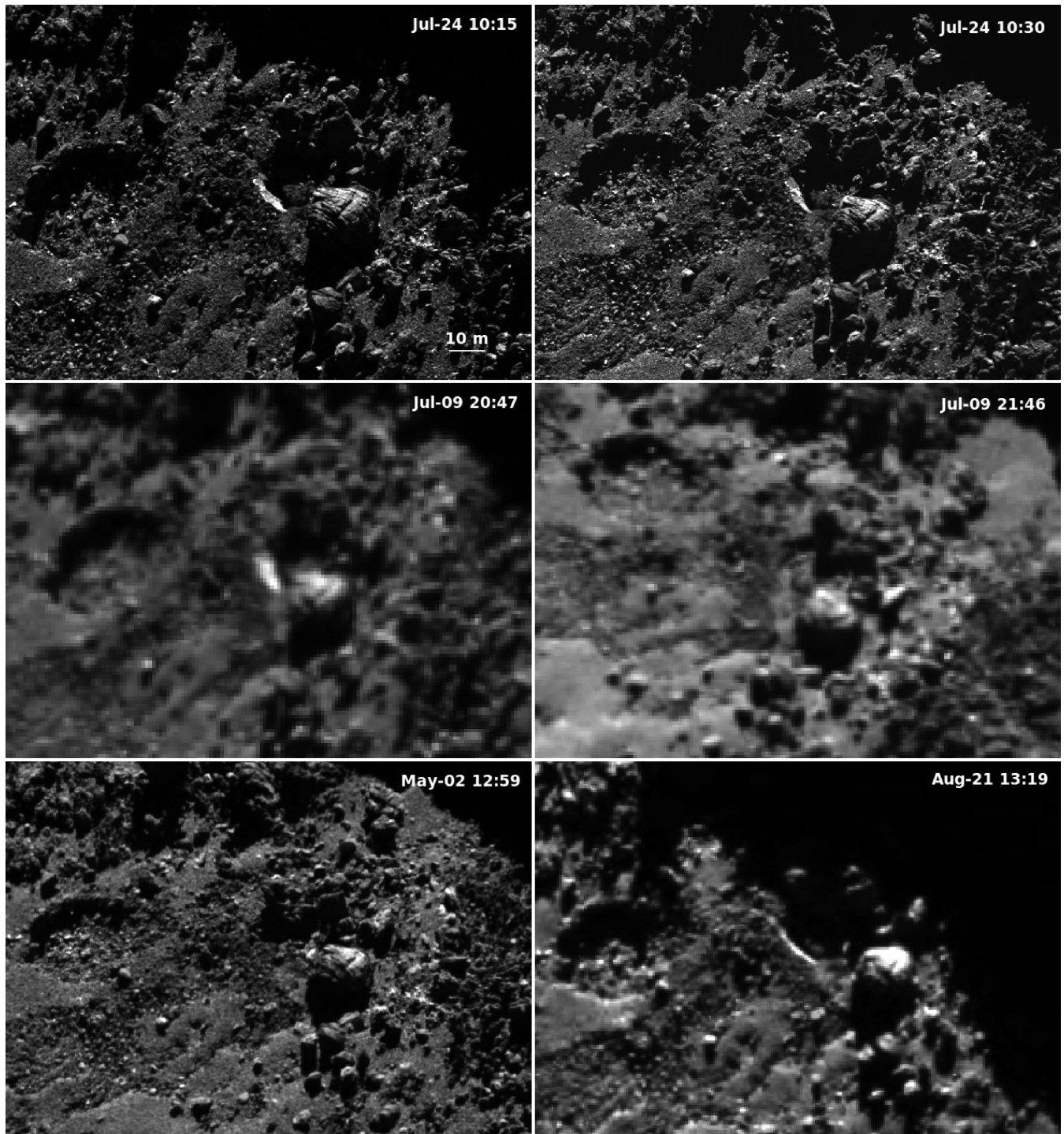
Figure A3. Images of the outburst site obtained between 2016 May 02 and August 21. The observation parameters are listed in Table 2. A bright patch at the site of the outburst was detected on July 09, 24 and August 21. The patch quickly enters shadow between 11:34 h and 13:23 local time, indicating a steep wall. The image of May 02 does not show the icy patch. It is the pre-outburst image matching most closely the viewing and illumination conditions of those showing the icy patch, although it was taken from a more shallow (by 3°) position. We use this image for a close comparison between pre- and post-outburst state of the source region in Fig. 13.

[1] *Max Planck Institute for Solar System Research, Justus-von-Liebig-Weg 3, D-37077 Göttingen, Germany*

[2] *Dipartimento di Scienze e Tecnologie, Università degli Studi di Napoli 'Parthenope', CDN, IC4, I-80143 Naples, Italy*

[3] *Institute for Space Astrophysics and Planetology, Via Fosso del Cavaliere 100, I-00133 Rome, Italy*

[4] *Department of Physics and Astronomy, The Johns Hopkins University, 3400 N. Charles Street, Baltimore, MD 21218, USA*

[5] *European Space Astronomy Centre, Camino bajo del Castillo s/n, E-28692 Villanueva de la Cañada, Spain*

[6] *Centro di Ateneo di Studi ed Attivitá Spaziali 'Giuseppe Colombo' (CISAS), University of Padova, Via Venezia 15, I-35131 Padova, Italy*

[7] *Department for Astronomy, University of Maryland, College Park, MD 20742, USA*

[8] *LESIA, Observatoire de Paris, PSL Research University, CNRS, Univ. Paris Diderot, Sorbonne Paris Cité, UPMC Univ. Paris 06, Sorbonne Universités, 5 Place J. Janssen, F-92195 Meudon Pricipal Cedex, France*

[9] *Max Planck Institute for Nuclear Physics, Saupfercheckweg 1, D-69117 Heidelberg, Germany*

[10] *Laboratory for Atmospheric and Space Physics, University of Colorado, 1234 Innovation Dr, Boulder, CO 80303, USA*

[11] *NASA Ames Research Center, Moffett Field, CA 94035, USA*

[12] *Department of Space Studies, Southwest Research Institute, Boulder, CO 80303, USA*

[13] *Physikalisches Institut, Sidlerstrasse 5, University of Bern, CH-3012 Bern, Switzerland*

[14] *Department of Physics and Astronomy 'G. Galilei', University of Padova, Vic. Osservatorio 3, I-35122 Padova, Italy*

[15] *LATMOS, CNRS/UVSQ/IPSL, 11 Boulevard d'Alembert, F-78280 Guyancourt, France*

[16] *INAF Osservatorio Astronomico di Padova, Vicolo dell'Osservatorio 5, I-35122 Padova, Italy*

[17] *CNR-IFN UOS Padova LUXOR, Via Trasea 7, I-35131 Padova, Italy*

[18] *Jet Propulsion Laboratory, M/S 183-401, 4800 Oak Grove Drive, Pasadena, CA 91109, USA*

[19] *Department of Industrial Engineering, University of Padova, Via Venezia 1, I-35131 Padova, Italy*

[20] *INAF - Osservatorio Astronomico di Trieste, Via Tiepolo 11, I-34143 Trieste, Italy*

[21] *Aix Marseille Université, CNRS, LAM (Laboratoire d'Astro-physique de Marseille) UMR 7326, F-13388 Marseille, France*

[22] *Instituto de Astrofisica de Andalucia-CSIC, Glorieta de la Astronomia, E-18008 Granada, Spain*

[23] *Universität der Bundeswehr LRT-7, Werner Heisenberg Weg 39, D-85577 Neubiberg, Germany*

[24] *Institute of Planetary Research, DLR, Rutherfordstrasse 2, D-12489 Berlin, Germany*

[25] *Institute of Astronomy, National Central University, 32054 Chung-Li, Taiwan*

[26] *Institute for Geophysics and Extraterrestrial Physics, TU Braunschweig, D-38106 Braunschweig, Germany*

[27] *von Hoerner und Sulger GmbH, Schlossplatz 8, D-68723 Schwetzingen, Germany*

[28] *Research and Scientific Support Department, European Space Agency, NL-2201 Noordwijk, the Netherlands*

[29] *Laboratoire d'Astrophysique de Marseille, UMR 7326 CNRS & Aix-Marseille Université, 38 rue Frédéric Joliot-Curie, F-13388 Marseille Cedex 13, France*

[30] *Instituto de Astrofisica de Andalucia-CSIC, Glorieta de la Astronomia, E-18008 Granada, Spain*

[31] *Centre for Astrophysics and Planetary Science, School of Physical Sciences, The University of Kent, Canterbury CT2 7NH, UK*

[32] *Department of Information Engineering, University of Padova, Via Gradenigo 6/B, I-35131 Padova, Italy*

[33] *Centro de Astrobiologia (INTA-CSIC), European Space Agency, European Space Astronomy Centre (ESAC), PO Box 78, E-28691 Villanueva de la Canada, Madrid, Spain*

[34] *International Space Science Institute, Hallerstrasse 6, CH-3012 Bern, Switzerland*

[35] *Finnish Meteorological Institute, Climate Research, Erik Palmenin aukio 1, PO Box 503, FI-00101 Helsinki, Finland*

[36] *Applied Physics Laboratory, Johns Hopkins University, Laurel, MD 20723, USA*

[37] *Department of Physics and Astronomy, Tuorla Observatory, University of Turku, Väisäläntie 20, FI-21500 Piikkiö, Finland*

This paper has been typeset from a TeX/LaTeX file prepared by the author.